Electronic Supporting Information (ESI)

Solvent mixtures for improved electron transfer kinetics of titanium-doped polyoxovanadate-alkoxide clusters

Mamta Dagar,[a] *Molly Corr,*[a] *Timothy R. Cook,*[b] *James R. Mckone**[c] *and Ellen M. Matson**[a]

[a]Department of Chemistry, University of Rochester, Rochester, NY 14627, USA

[b]Department of Chemistry, University at Buffalo, The State University of New York, Buffalo NY 14260, USA

[c]Department of Chemical and Petroleum Engineering, University of Pittsburgh, PA 15261, USA

Corresponding author email: jmckone@pitt.edu, matson@chem.rochester.edu

Supporting Information Table of Contents

Experimental methods:

General considerations. All manipulations were carried out in the absence of water and oxygen in a UniLab MBraun inert atmosphere glovebox under a dinitrogen atmosphere. Glassware was oven dried for a minimum of 4 hours and cooled in an evacuated antechamber prior to use in the drybox. Anhydrous methanol was purchased from Sigma-Aldrich and stored over activated 4 Å molecular sieves purchased from Fisher Scientific. All other solvents were dried and deoxygenated on a Glass Contour System (Pure

Process Technology, LLC) and stored over activated 3 Å molecular sieves purchased from Fisher Scientific. [^{n}Bu$_4$N][PF$_6$] was purchased from Sigma-Aldrich, recrystallized thrice using hot methanol, and stored under dynamic vacuum for a minimum of two days prior to use. [$Ti_2V_4O_5(OMe)_{14}$] was synthesized according to previous literature.[1] All electrochemical experiments were conducted in the glove box using either a Bio-Logic SP 150 potentiostat/galvanostat or a Bio-Logic SP 300 potentiostat/galvanostat and the EC-Lab software suite.

Determining D_0. 5 mM concentration of [$Ti_2V_4O_5(OMe)_{14}$] with 0.1 M [^{n}Bu$_4$N][PF$_6$] as the supporting electrolyte were used for all experiments. CV measurements were carried out inside a nitrogen filled glove box (MBraun, USA) using a Bio-Logic SP 150 potentiostat/galvanostat and the EC-Lab software suite. Cyclic voltammograms were recorded using a 3 mm diameter glassy carbon working electrode (CH Instruments, USA), a Pt wire auxiliary electrode (CH Instruments, USA), and a Ag/Ag^+ non-aqueous reference electrode with 0.01 M $AgNO_3$ in 0.1 M [^{n}Bu$_4$N][PF$_6$]in CH_3CN (Bio-Logic). Cyclic voltammograms were *iR* compensated at 95% with impedance taken at 100 kHz using the ZIR tool included within the EC-Lab software.

The diffusion coefficient associated with each redox couple was determined by using the slope of the peak current (i_P) versus the square root of scan rate $\nu^{1/2}$. The Randles – Sevcik equation was used to estimate the diffusion coefficients from CV data. For a reversible redox couple, the peak current is given by the eq. S1 –

$$i_p = 2.69 \times 10^5 \, n^{3/2} \, A \, c \, D_0^{1/2} \, \nu^{1/2} \qquad \text{Eq. S1}$$

In eq. S1, n is the number of electrons transferred; A is the electrode area (0.0707 cm^2 for the glassy carbon working electrode); c is the bulk concentration of the active species; D_0 is the diffusion coefficient of the active species; ν is the scan rate. For an irreversible redox couple, the peak current, is given by the eq. S2:

$$i_p = 2.99 \times 10^5 \, n^{3/2} \, \alpha^{1/2} A \, c \, D_0^{1/2} \, \nu^{1/2} \qquad \text{Eq. S2}$$

where α is the charge transfer coefficient. For this study, α = 0.5.

For the redox couples that show quasi-reversible kinetics, relationships for both reversible and irreversible redox reaction are usually employed to determine the diffusion coefficients of such redox processes. Therefore, an average value of diffusion coefficient was approximated for a quasi-reversible redox couple using both equations S1 and S2.[2-4]

Calculation of k_0. The electron-transfer kinetics was estimated directly from CV measurements by using the Nicholson method.[5] The potential difference (ΔEp) of oxidation and reduction peaks were obtained at different scan rates. The transfer parameter, ψ, was extracted from the working curve constructed by Nicholson using ΔEp values. The standard heterogeneous charge-transfer rate constant, k_0, for a given electron transfer process was determined using the following equation:

$$\Psi = \nu^{-1/2} k_0 \left({}^{\pi n F D_0}/_{RT} \right)^{-1/2}$$

where n is the number of electrons transferred, F is the Faraday constant, D is the diffusion coefficient, ν is the scan rate, R is the ideal gas constant and T is the temperature.

Viscosity and conductivity measurements. The viscosity and conductivity of the electrolyte was determined using the Stokes – Einstein (Eq. S3) and Nernst – Einstein equations (Eq. S4), respectively.

$$\eta = \frac{k_B T}{6\pi D r} \qquad \text{Eq. S3}$$

where η is the viscosity of the electrolyte, k_B is the Boltzmann constant, T is the temperature, D is the diffusion coefficient, and r is the radius of the cluster. The viscosity values were calculated using the diffusion coefficient for the **+1/0** and **0/-1** redox couples and averaged to obtain the viscosity for the given solvent system.

$$\lambda = \frac{z_i^2 F^2}{RT}(D_+ + D_-) \qquad \text{Eq. S4}$$

where λ is the conductivity, z_i is the charge on the cluster, F is the Faraday constant, R is the ideal gas constant, T is the temperature, and D_+ and D_- are the diffusivities of the **+1/0** and **0/-1** redox couples, respectively.

Error calculations:

The errors were calculated using the Data Analysis software package (MS Excel) unless otherwise specified. A regression analysis was performed on the linear fit using 95 % confidence interval and the obtained values of the standard error were multiplied by the relevant coefficient in a given formula. An example calculation is shown below –

To obtain the diffusion coefficient of the **+1/0** redox couple in MeCN, a plot of peak current (i_P) versus the square root of scan rate $\nu^{1/2}$ was sketched and the slope was used to calculate D_0. The Randles – Sevcik equation can be rearranged as –

$$Slope = 2.69 \times 10^5 \, n^{3/2} \, A \, c \, D_0^{1/2}$$

Rearranging the equation to obtain D_0 –

$$D_0 = \frac{Slope}{2.69 \times 10^5 \, n^{3/2} \, A \, c} \qquad \text{Eq. S5}$$

Here, n = 1, A = 0.0707 cm^2 and c = 0.005 M

Similarly, for an irreversible redox couple –

$$D_0 = \frac{Slope}{2.99 \times 10^5 \, n^{3/2} \, \alpha^{1/2} \, A \, c} \qquad \text{Eq. S6}$$

where α = 0.5

The output file from the regression analysis is included below.

Regression Statistics

Multiple R	0.999969
R Square	0.999938
Adjusted R Square	0.933271

Standard Error	4.07E-06
Observations	16

	df	***SS***	***MS***	***F***	***Significance F***
Regression	1	4E-06	4E-06	241637.9	4.59E-31
Residual	15	2.48E-10	1.65E-11		
Total	16	4E-06			

	Coefficients	***Standard Error***	***t Stat***	***P-value***	***Lower 95%***	***Upper 95%***	***Lower 95.0%***	***Upper 95.0%***
Intercept	0	#N/A	#N/A	#N/A	#N/A	#N/A	#N/A	#N/A
X Variable	0.000265	5.39E-07	491.5668	5.67E-33	0.000264	0.000266	0.000264	0.000266

After obtaining the required statistics, the standard error on the slope in the upper and lower 95 % confidence interval were plugged in Eq. S5 and Eq. S6 to get a positive and negative error value for the reversible and irreversible D_0 values. The quasi reversible D_0 values were finally obtained by averaging them. The results for **+1/0** redox couple are tabulated below.

	Upper 95%	**Lower 95%**
Reversible	7.78×10^{-6} cm^2/s	7.71×10^{-6} cm^2/s
Irreversible	1.26×10^{-5} cm^2/s	1.25×10^{-5} cm^2/s
Quasi – reversible	1.02×10^{-5} cm^2/s	1.01×10^{-5} cm^2/s

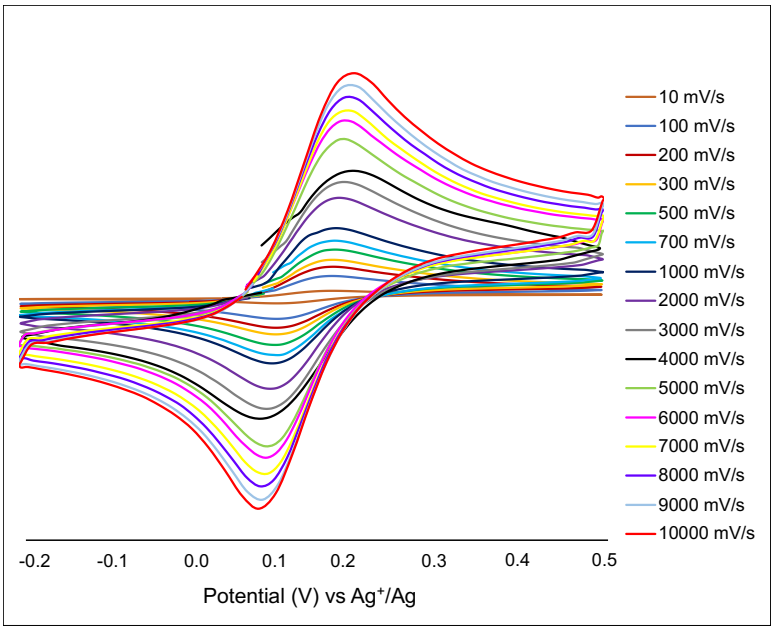

Figure S1. Cyclic voltammograms of $\mathbf{1}^{+}/\mathbf{0}$ redox couple at scan rates ranging from 10 – 10000 mV/s in MeCN.

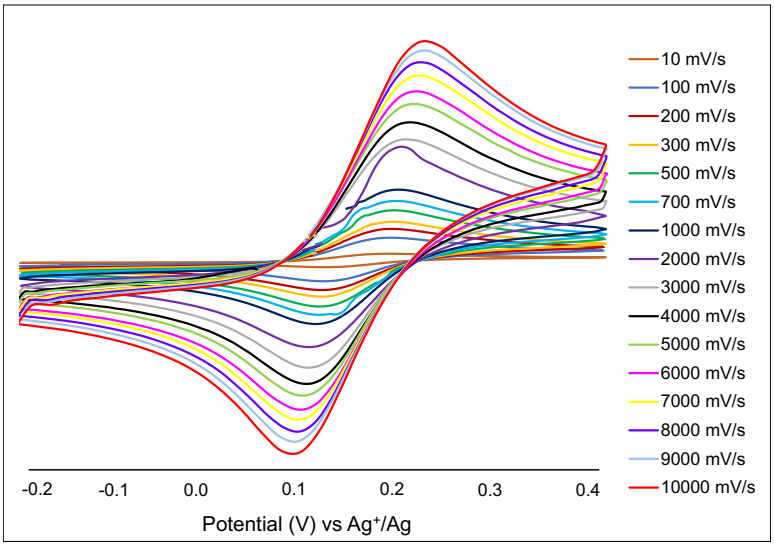

Figure S2. Cyclic voltammograms of $\mathbf{1}^{+}/\mathbf{0}$ redox couple at scan rates ranging from 10 – 10000 mV/s in DMF.

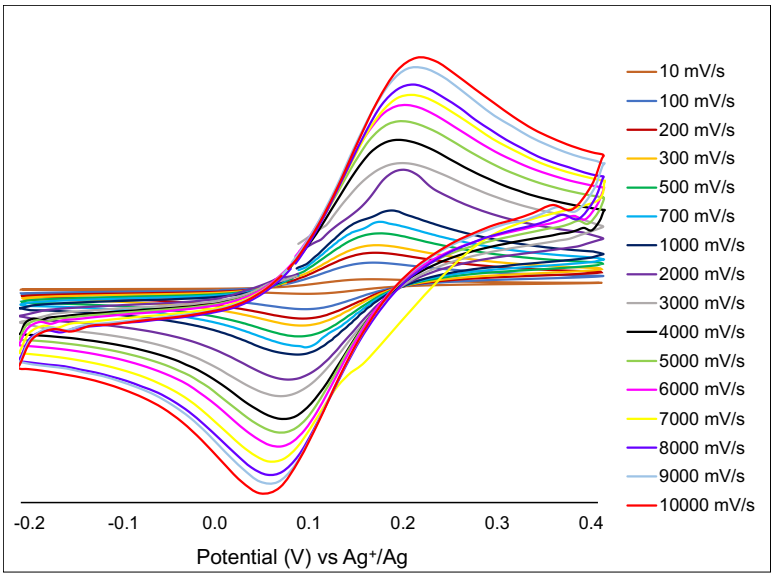

Figure S3. Cyclic voltammograms of $\mathbf{1}^{+}/\mathbf{0}$ redox couple at scan rates ranging from 10 – 10000 mV/s in DMSO.

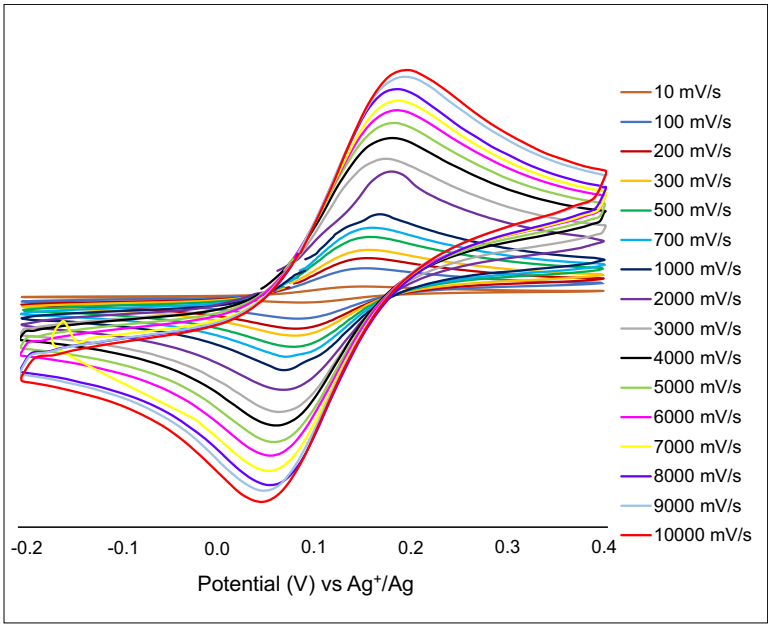

Figure S4. Cyclic voltammograms of $\mathbf{1}^{+}/\mathbf{0}$ redox couple at scan rates ranging from 10 – 10000 mV/s in PC.

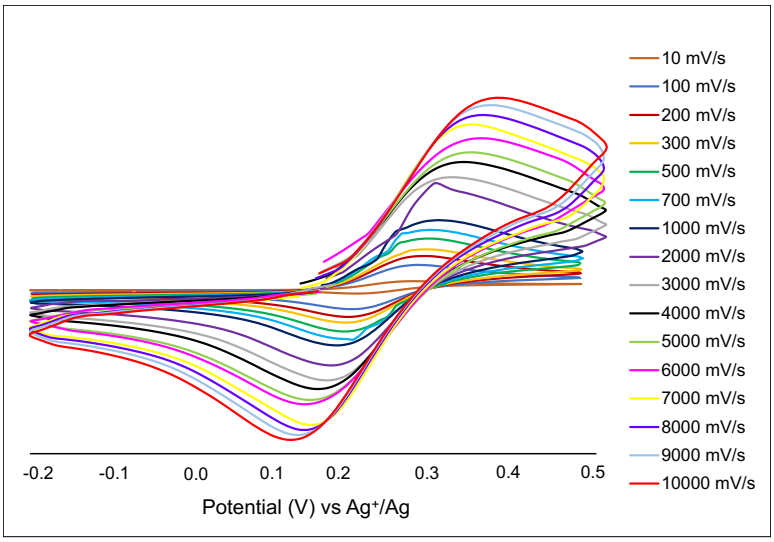

Figure S5. Cyclic voltammograms of $\mathbf{1}^{+}/\mathbf{0}$ redox couple at scan rates ranging from 10 – 10000 mV/s in DCM.

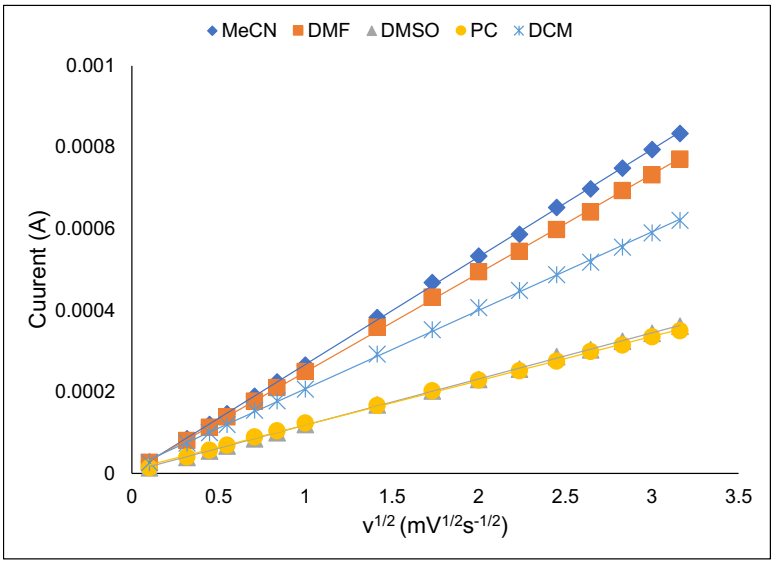

Figure S6. Plots of the square root of scan rate *versus* the peak current for $\mathbf{1}^{+}/\mathbf{0}$ redox couple in different solvents.

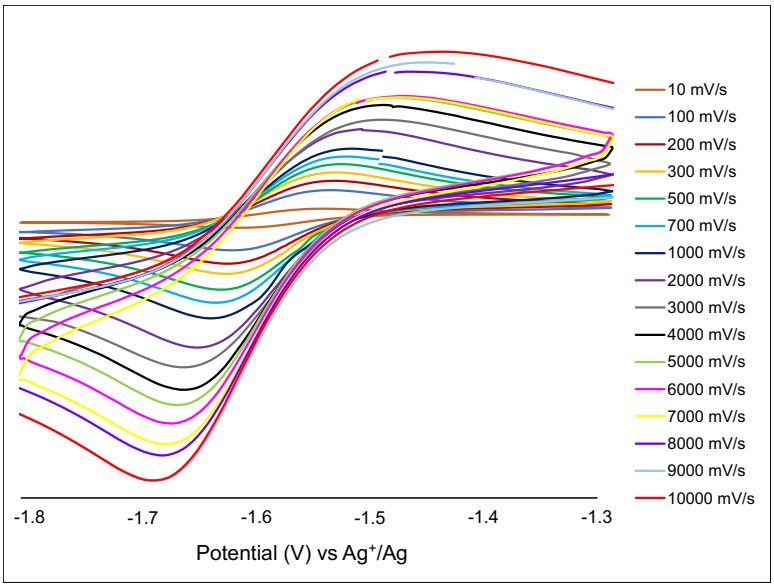

Figure S7. Cyclic voltammograms of **0/1**$^{-}$ redox couple at scan rates ranging from 10 – 10000 mV/s in MeCN.

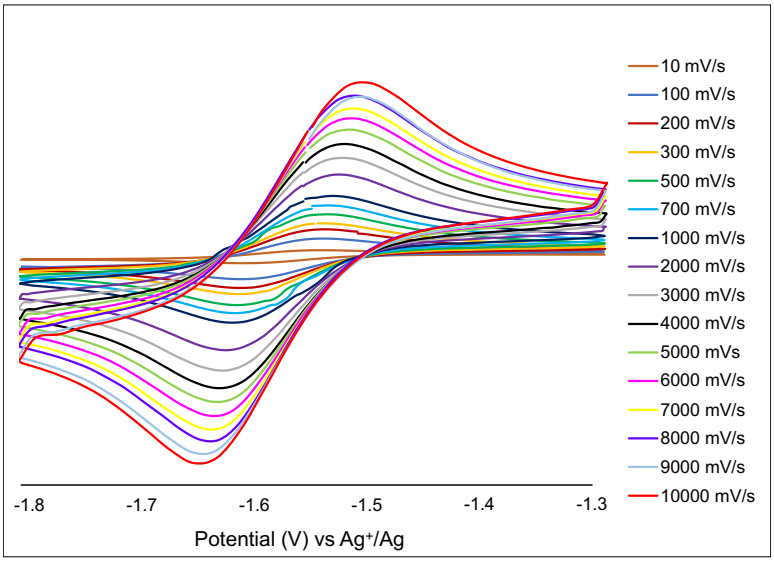

Figure S8. Cyclic voltammograms of **0/1**$^{-}$ redox couple at scan rates ranging from 10 – 10000 mV/s in DMF.

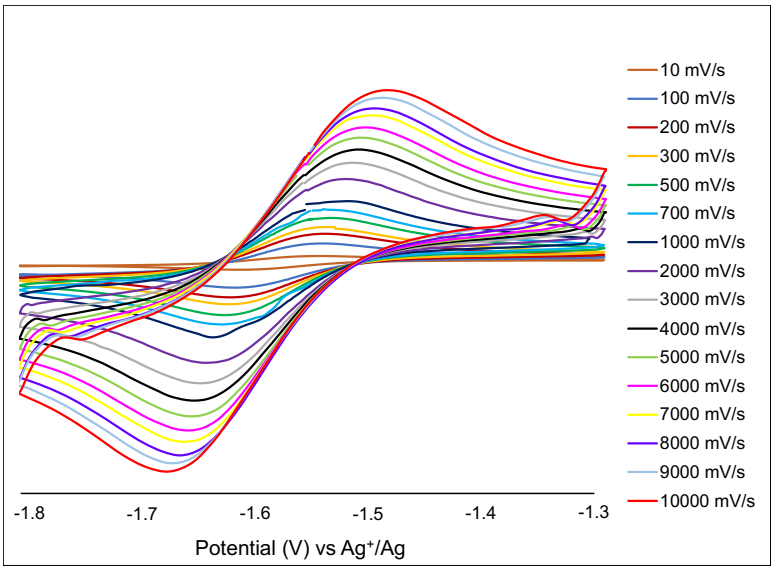

Figure S9. Cyclic voltammograms of **0/1**$^{-}$ redox couple at scan rates ranging from 10 – 10000 mV/s in DMSO.

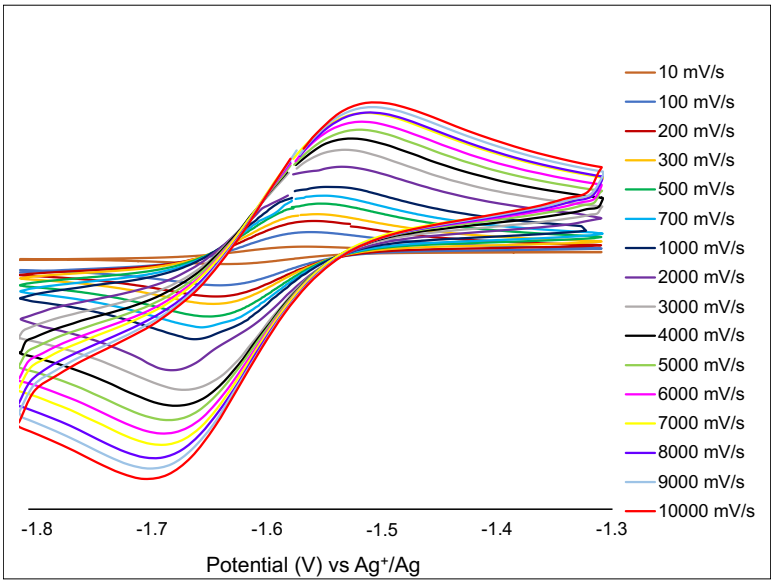

Figure S10. Cyclic voltammograms of **0/1**$^{-}$ redox couple at scan rates ranging from 10 – 10000 mV/s in PC.

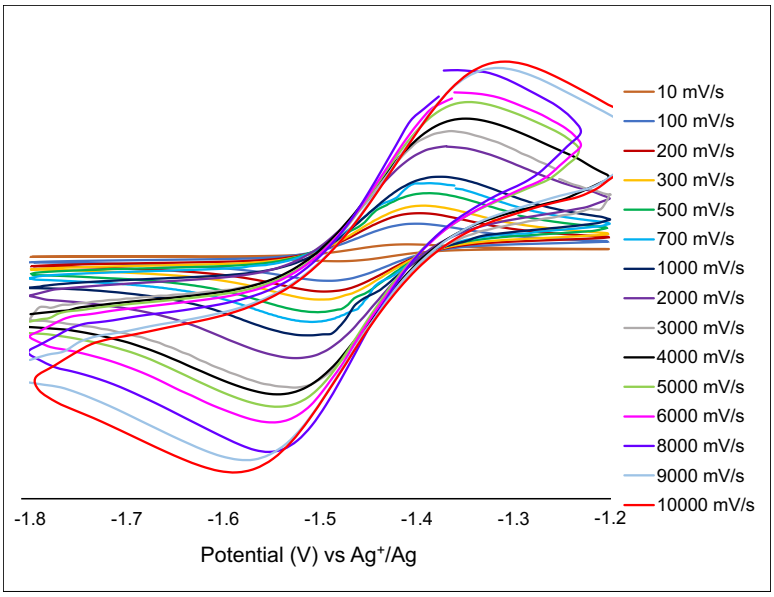

Figure S11. Cyclic voltammograms of **0/1**$^{-}$ redox couple at scan rates ranging from 10 – 10000 mV/s in DCM.

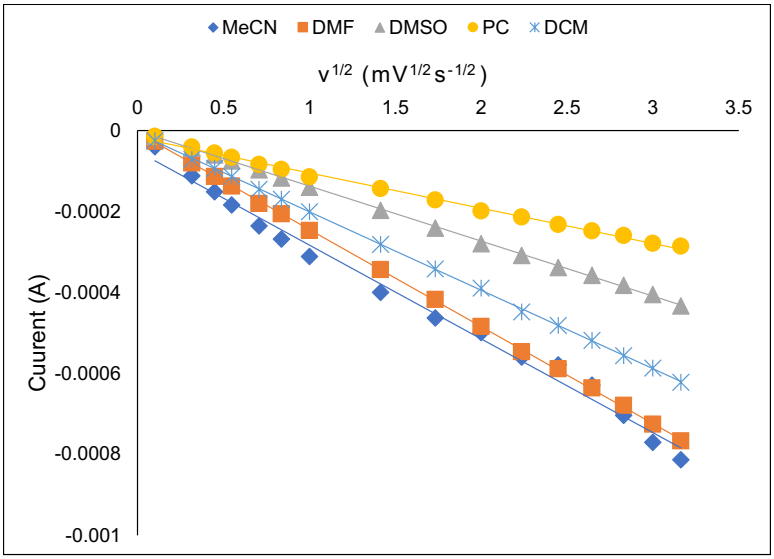

Figure S12. Plots of the square root of scan rate *versus* the peak current for **0/1**$^{-}$ redox couple in different solvents.

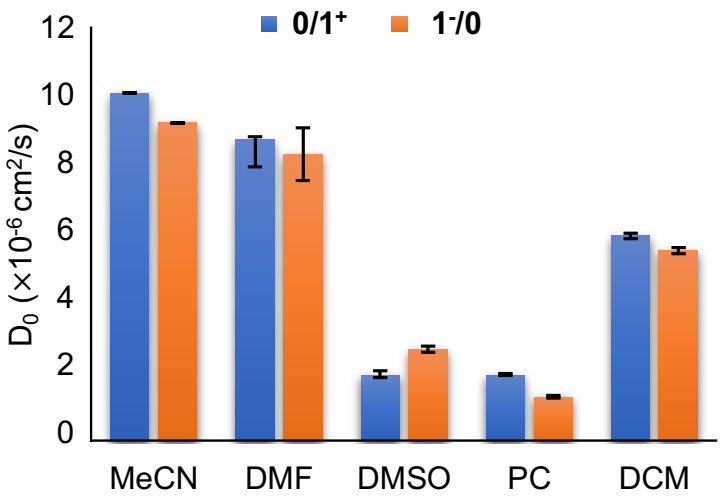

Figure S13. Comparison of diffusion coefficients of the neutral species in different solvents. The blue bars represent the one electron oxidation of the neutral cluster, whereas the orange bars represent the one electron reduction of the neutral complex. Both values in each individual solvent systems are similar within experimental error range. This is indicative of the fact that the forward sweeps in the cyclic voltammograms give the diffusivity values for the neutral species, and hence should give the same D_0.

Table S1. Comparison of experimentally obtained diffusion coefficients of neutral and charged $[Ti_2V_4O_5(OMe)_{14}]$. O = D_0 calculated from oxidative wave; R = D_0 calculated from reductive wave.

Solvent	D_0 (neutral) (cm^2/s)	D_0 (+1 oxidation state) (cm^2/s)	D_0 (-1 oxidation state) (cm^2/s)
MeCN	O: $10.3 \pm 0.08 \times 10^{-6}$ R: $9.4 \pm 0.78 \times 10^{-6}$	$9.6 \pm 0.23 \times 10^{-6}$	$3.7 \pm 0.84 \times 10^{-6}$
DMF	O: $8.9 \pm 0.10 \times 10^{-6}$ R: $8.5 \pm 0.08 \times 10^{-6}$	$6.5 \pm 0.25 \times 10^{-6}$	$6.7 \pm 0.41 \times 10^{-6}$
DMSO	O: $1.9 \pm 0.03 \times 10^{-6}$ R: $2.7 \pm 0.04 \times 10^{-6}$	$1.6 \pm 0.06 \times 10^{-6}$	$1.8 \pm 0.15 \times 10^{-6}$
PC	O: $1.9 \pm 0.06 \times 10^{-6}$ R: $1.3 \pm 0.09 \times 10^{-6}$	$1.4 \pm 0.08 \times 10^{-6}$	$1.0 \pm 0.11 \times 10^{-6}$
DCM	O: $6.1 \pm 0.15 \times 10^{-6}$ R: $5.6 \pm 0.08 \times 10^{-6}$	$4.5 \pm 0.29 \times 10^{-6}$	$5.2 \pm 0.33 \times 10^{-6}$

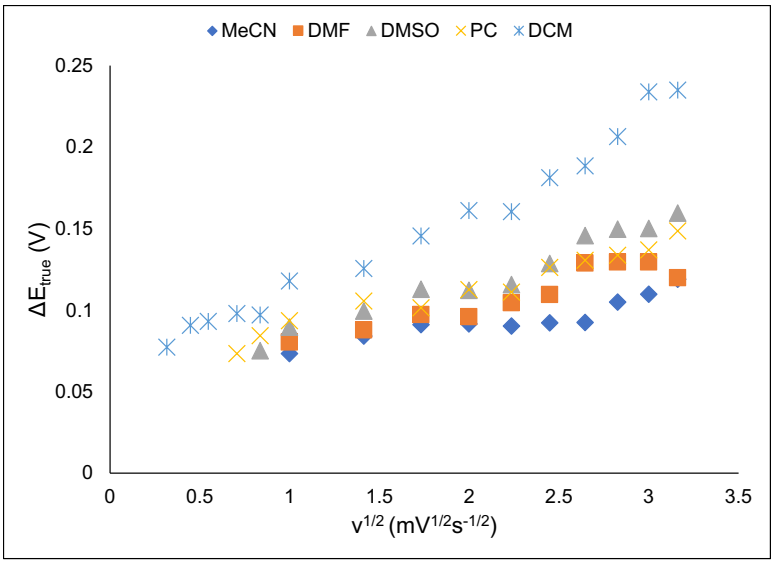

Figure S14. Plot of peak-to-peak separation (ΔE_p) *versus* square root of scan rate for $\mathbf{1}^+/\mathbf{0}$ redox couple in different solvents. For each solvent, values are included for the scan rate range where $\Delta E_p > 64$ mV and increases as a function of scan rate.

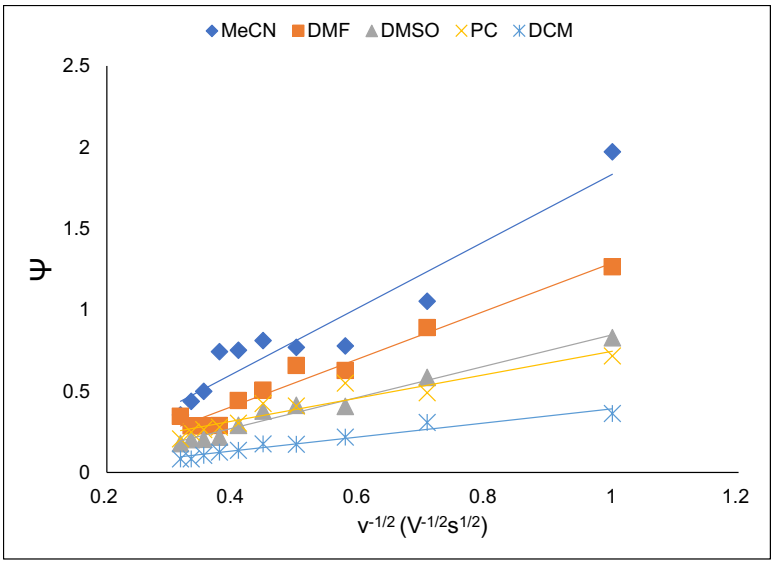

Figure S15. Plot of Nicholson parameter (Ψ) *versus* inverse square root of scan rate for $\mathbf{1}^+/\mathbf{0}$ redox couple in different solvents. For each solvent, Ψ values corresponding to the given ΔE_p are included for scan rates where $\Delta E_p > 64$ mV.

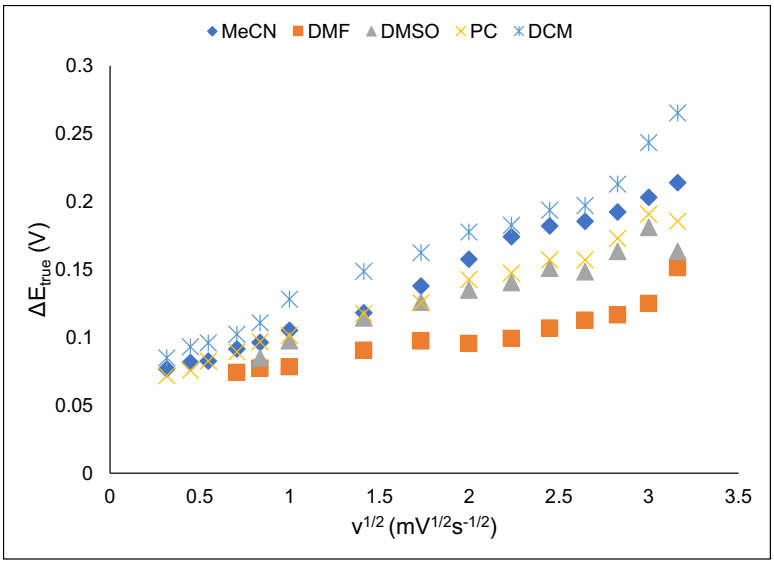

Figure S16. Plot of peak-to-peak separation (ΔE_p) *versus* square root of scan rate for **0/1**$^-$ redox couple in different solvents. For each solvent, values are included for the scan rate range where $\Delta E_p > 64$ mV and increases as a function of scan rate.

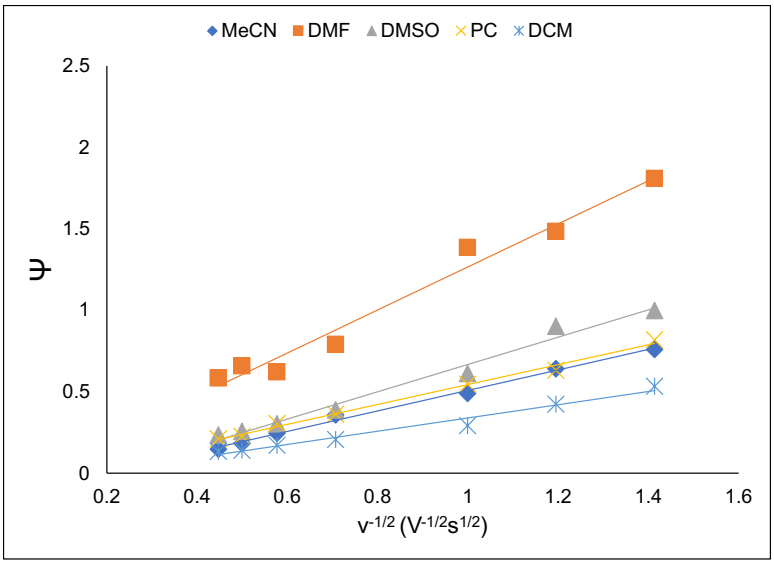

Figure S17. Plot of Nicholson parameter (Ψ) *versus* inverse square root of scan rate for **0/1**$^-$ redox couple in different solvents. For each solvent, Ψ values corresponding to the given ΔE_p are included for scan rates where $\Delta E_p > 64$ mV.

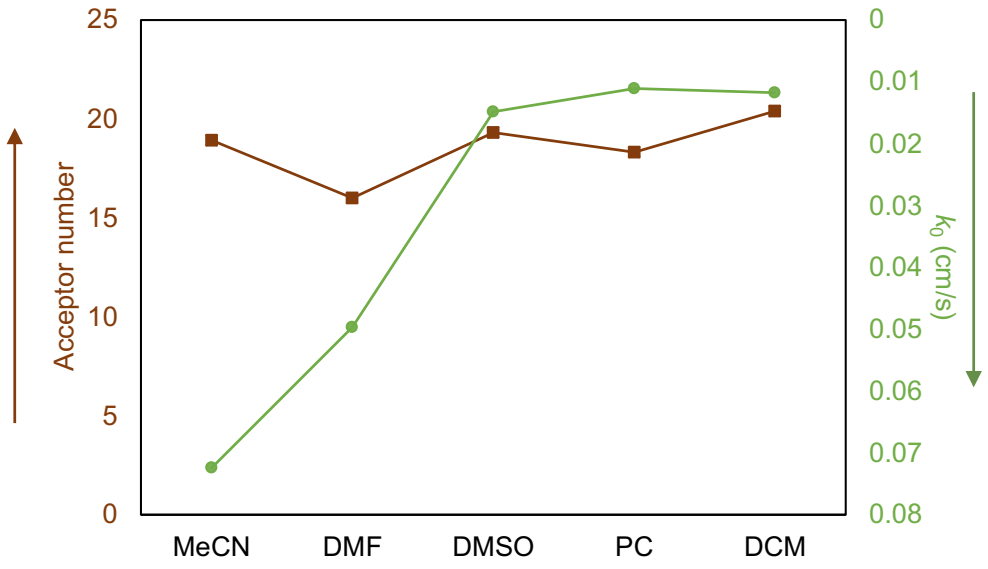

Figure S18. Comparison of k_0 for $\mathbf{1}^{+}/\mathbf{0}$ redox couple to solvents' acceptor number.

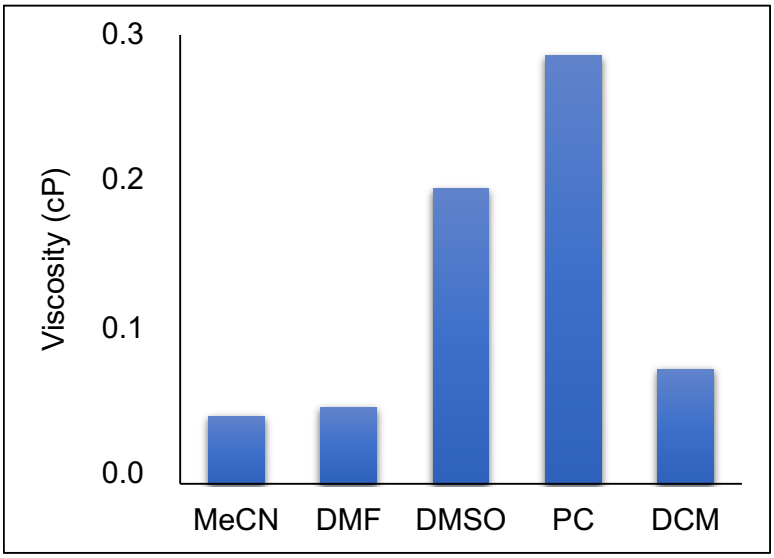

Figure S19. Viscosity of the electrolyte in different solvents calculated using Stokes – Einstein equation.

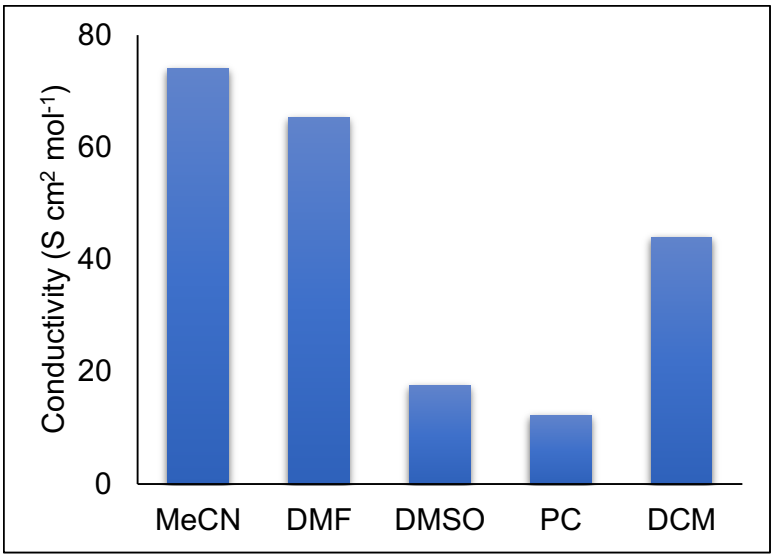

Figure S20. Conductivity of the electrolyte in different solvents calculated using Nernst – Einstein equation.

Bulk oxidation in pure solvent

Based on our initial analysis of the role of solvent on diffusivity and kinetics of the charge carrier [$Ti_2V_4O_5(OMe)_{14}$], we explored the electrochemical stability of the cluster in each solvent. For [$Ti_2V_4O_5(OCH_3)_{14}$] to be a viable charge carrier for symmetric RFBs, it is crucial that the cluster exhibits electrochemical stability across the +1 and -1 charge states, as these are the redox events accessed during battery cycling. To evaluate the stability of the charge carrier in its reduced and oxidized forms, bulk electrolysis was conducted at the specified potentials for each of the solvent systems.

Table S2. Potential values utilized for bulk electrolysis in different solvents.

Solvent	Potential used for bulk oxidation (V)	Potential used for bulk reduction (V)
MeCN	+0.6	-1.7
PC	+0.6	-1.75
DCM	+0.46	-1.73

Bulk oxidation of [$Ti_2V_4O_5(OMe)_{14}$] in DMSO and DMF results in significant degradation of the cluster over the course of the experiment. This indicates that although the transport properties are competitive for [$Ti_2V_4O_5(OCH_3)_{14}$] in DMSO and DMF, the instability of the assembly under the oxidizing conditions required for cell cycling render these solvents unfit for battery design. In contrast, as depicted in Figure S21-S22, bulk electrolysis of [$Ti_2V_4O_5(OMe)_{14}$] in MeCN, DCM, and PC revealed successful oxidation and reduction of the metal oxide cluster. Moreover, no cluster degradation was observed in these solvents as indicated by the CVs taken immediately post bulk electrolysis.

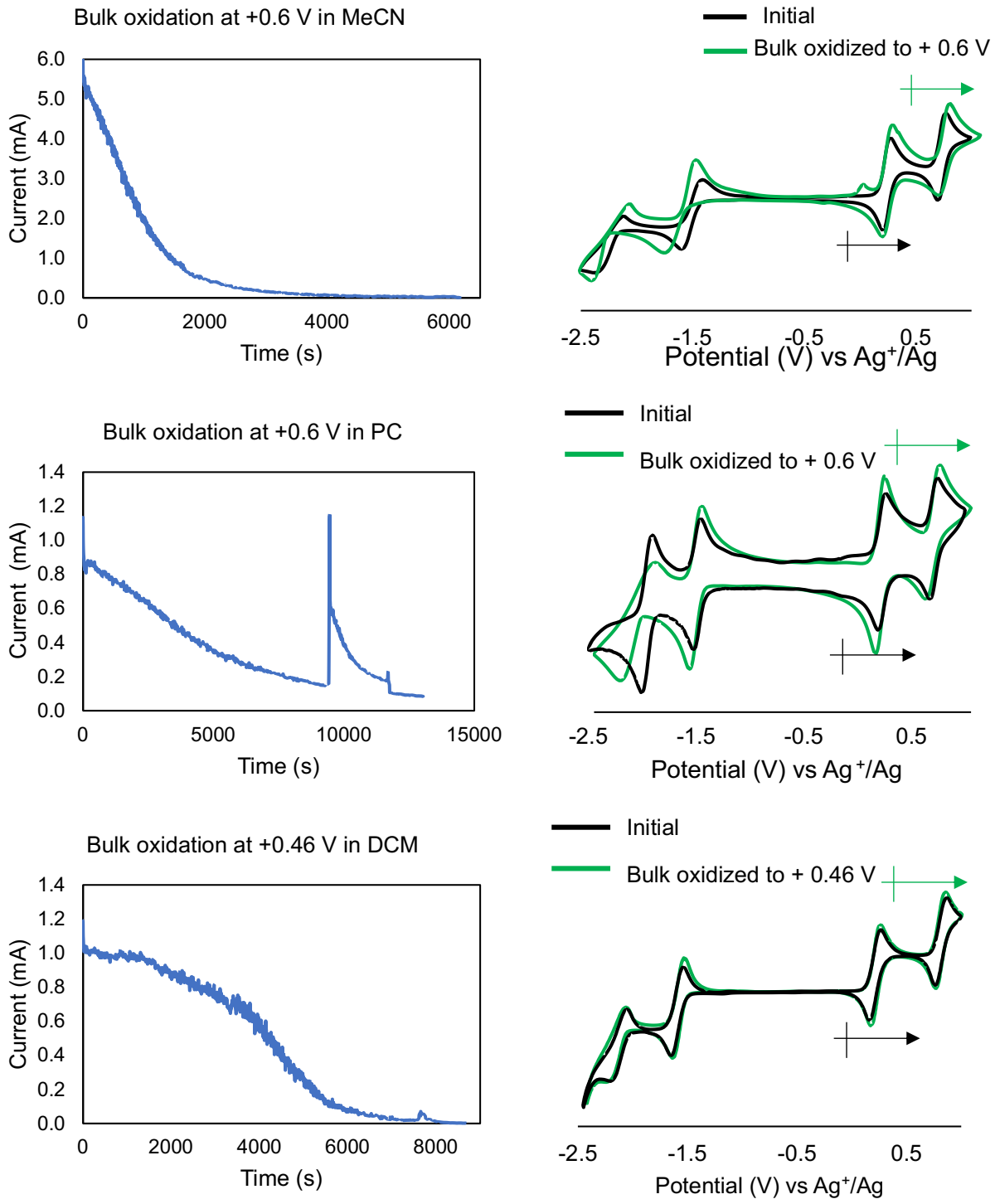

Figure S21. Bulk oxidation curves in MeCN, PC, and DCM (left); pre and post CV analysis of the electrolyte (right). All spurious responses in the bulk oxidation plots are due to the stir bar getting stuck in between the sides of the electrochemical cell and the electrodes.

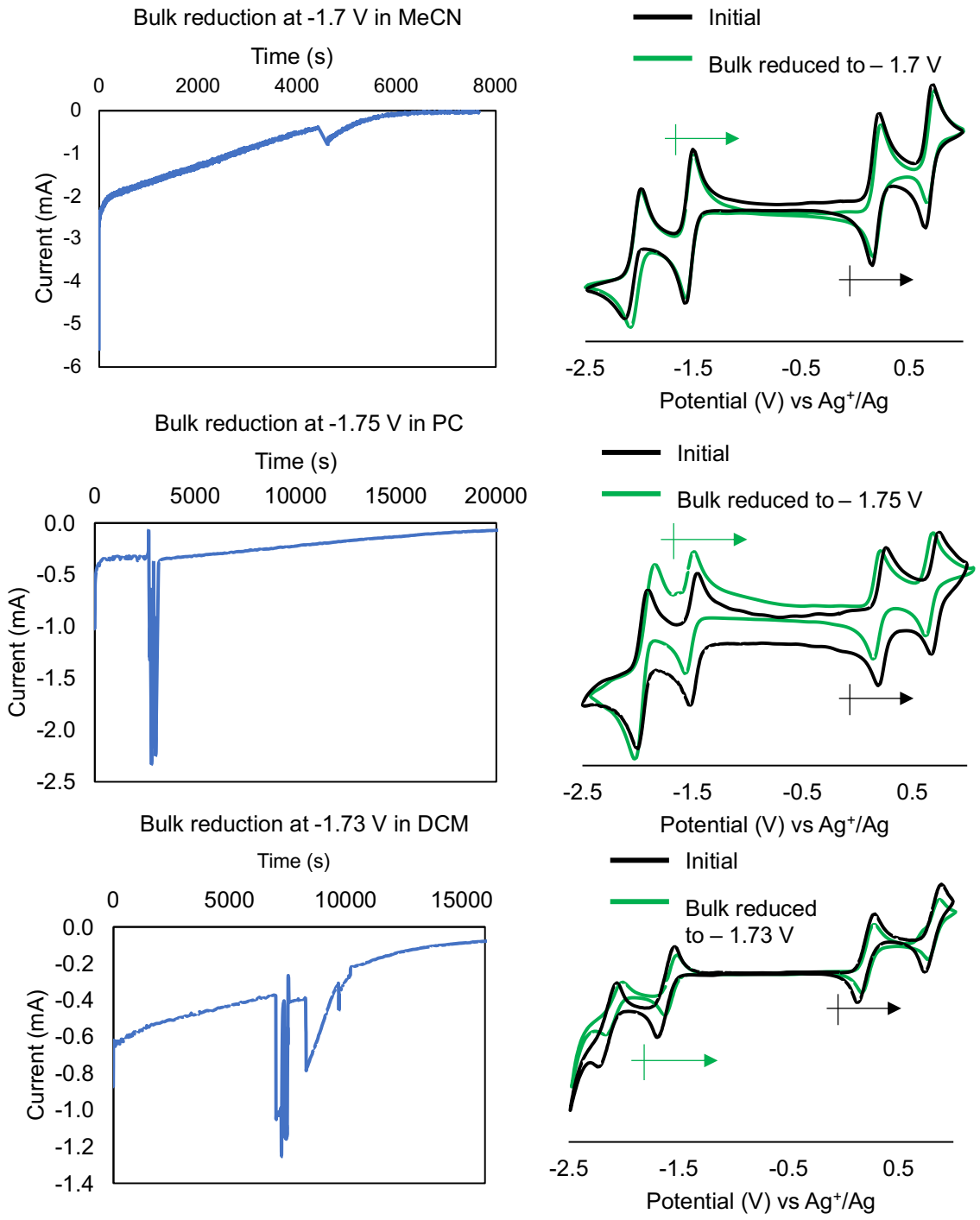

Figure S22. Bulk reduction curves in MeCN, PC, and DCM (left); pre and post CV analysis of the electrolyte (right). All spurious responses in the bulk reduction plots are due to the stir bar getting stuck in between the sides of the electrochemical cell and the electrodes.

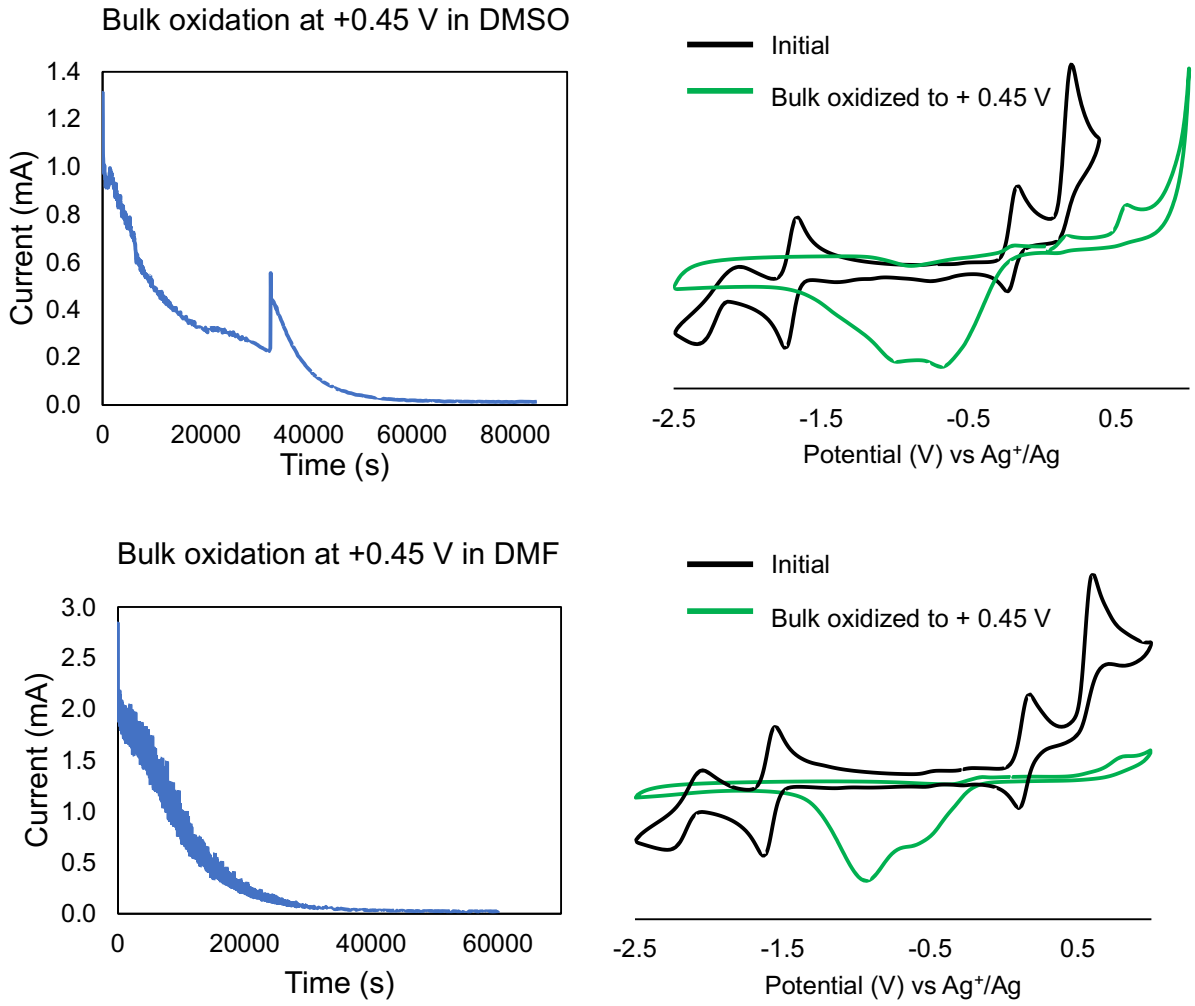

Figure S23. Bulk oxidation curves in DMSO (top) and DMF (bottom); pre and post CV analysis of the electrolyte (right). The green traces of the bulk oxidized electrolyte demonstrate the oxidative instability in +1 oxidation state of $[Ti_2V_4O_5(OMe)_{14}]$. All spurious responses in the bulk oxidation plot of DMSO are due to the stir bar getting stuck in between the sides of the electrochemical cell and the electrodes.

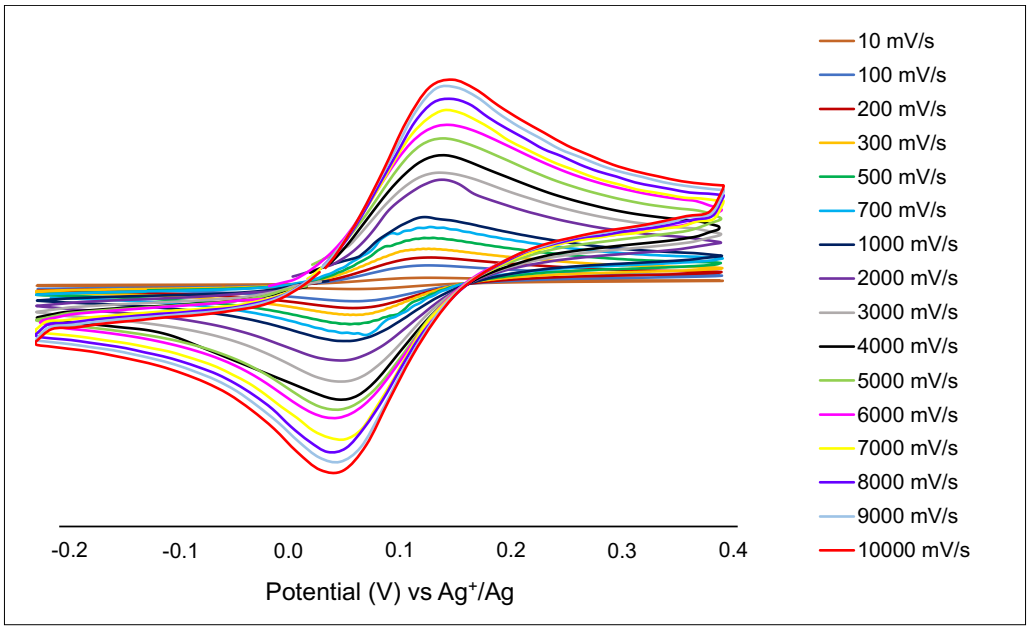

Figure S24. Cyclic voltammograms of $\mathbf{1}^{+}/\mathbf{0}$ redox couple at scan rates ranging from 10 – 10000 mV/s in 80:20 (v/v) MeCN:PC.

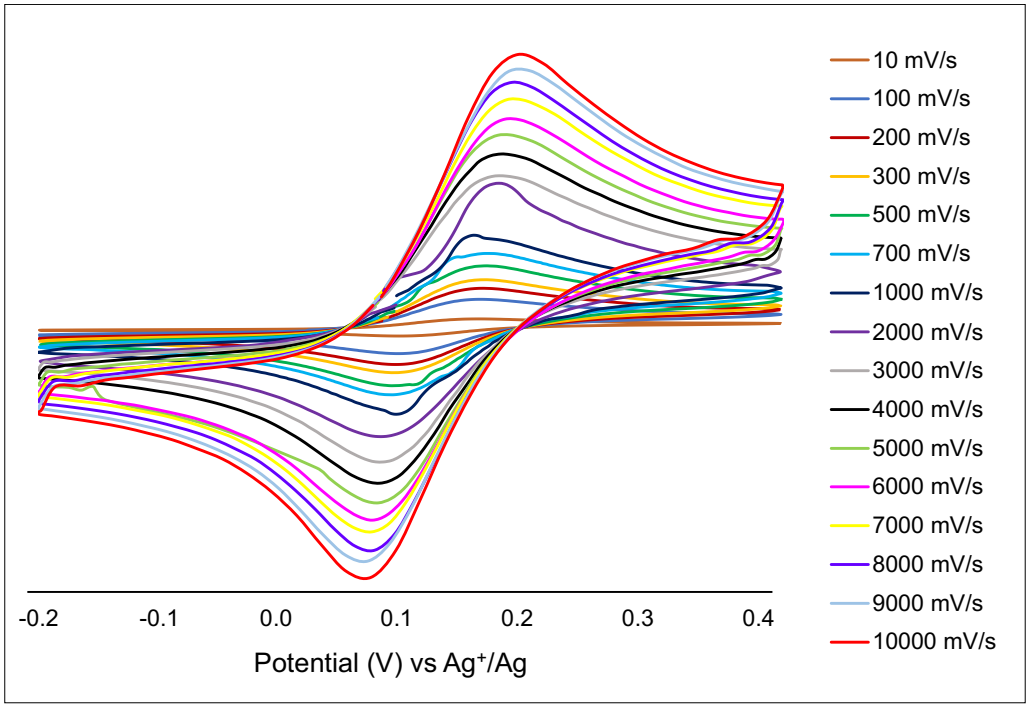

Figure S25. Cyclic voltammograms of $\mathbf{1}^{+}/\mathbf{0}$ redox couple at scan rates ranging from 10 – 10000 mV/s in 50:50 (v/v) MeCN:PC.

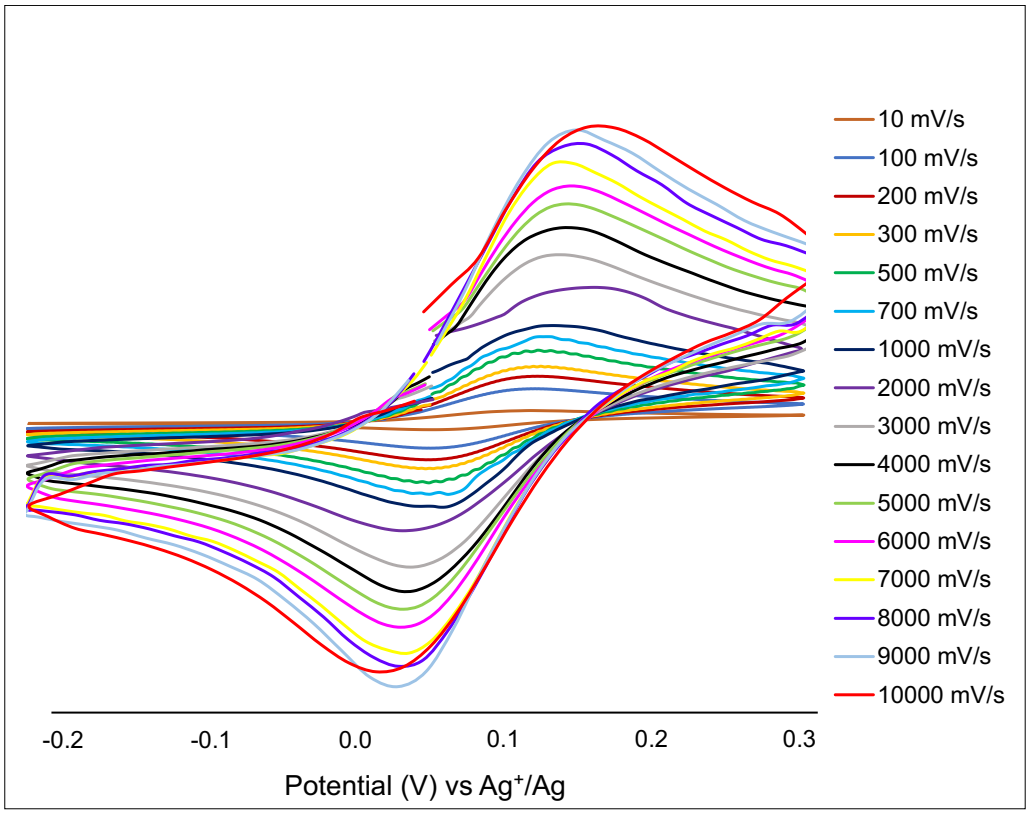

Figure S26. Cyclic voltammograms of $\mathbf{1}^{+}/\mathbf{0}$ redox couple at scan rates ranging from 10 – 10000 mV/s in 20:80 (v/v) MeCN:PC.

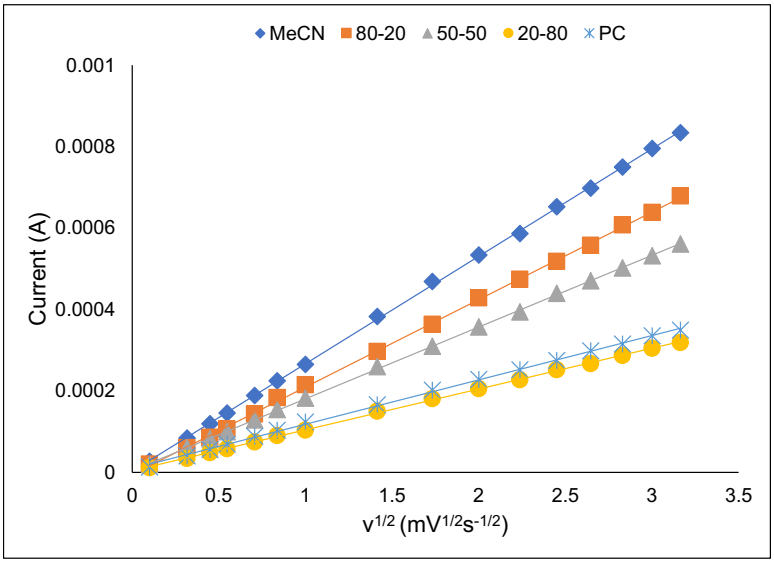

Figure S27. Plots of the square root of scan rate *versus* the peak current for $\mathbf{1}^{+}/\mathbf{0}$ redox couple in MeCN – PC mixtures. In the legend, the concentration of PC increases from left to right. For instance, ■ represents 80:20 (v/v) MeCN:PC mixture.

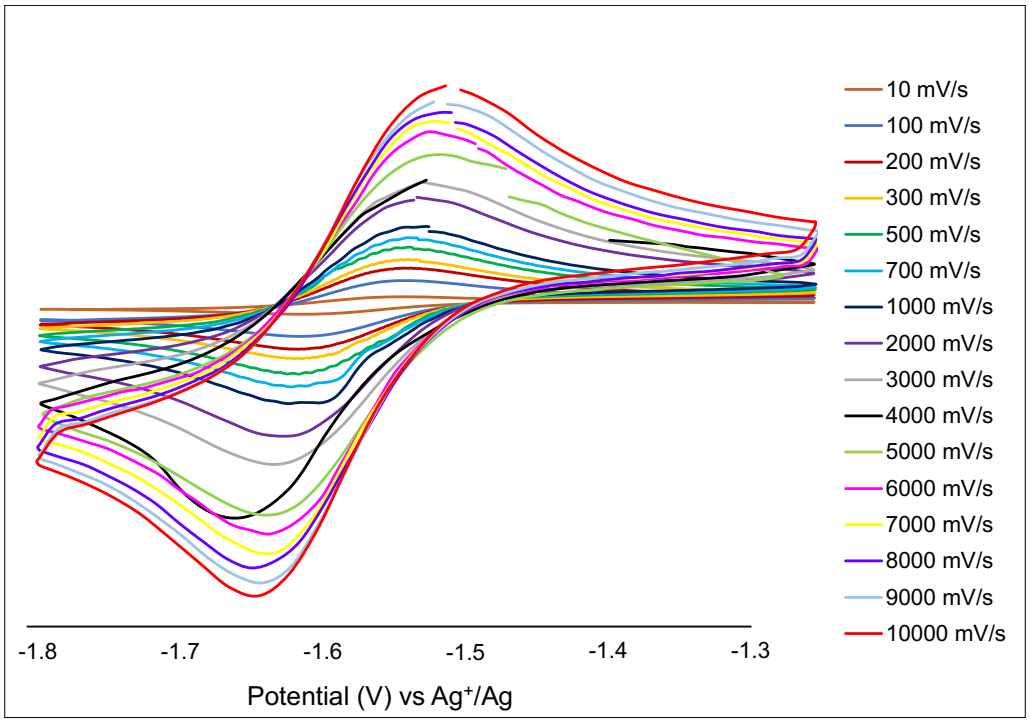

Figure S28. Cyclic voltammograms of **0/1**$^{-}$ redox couple at scan rates ranging from 10 – 10000 mV/s in 80:20 (v/v) MeCN:PC.

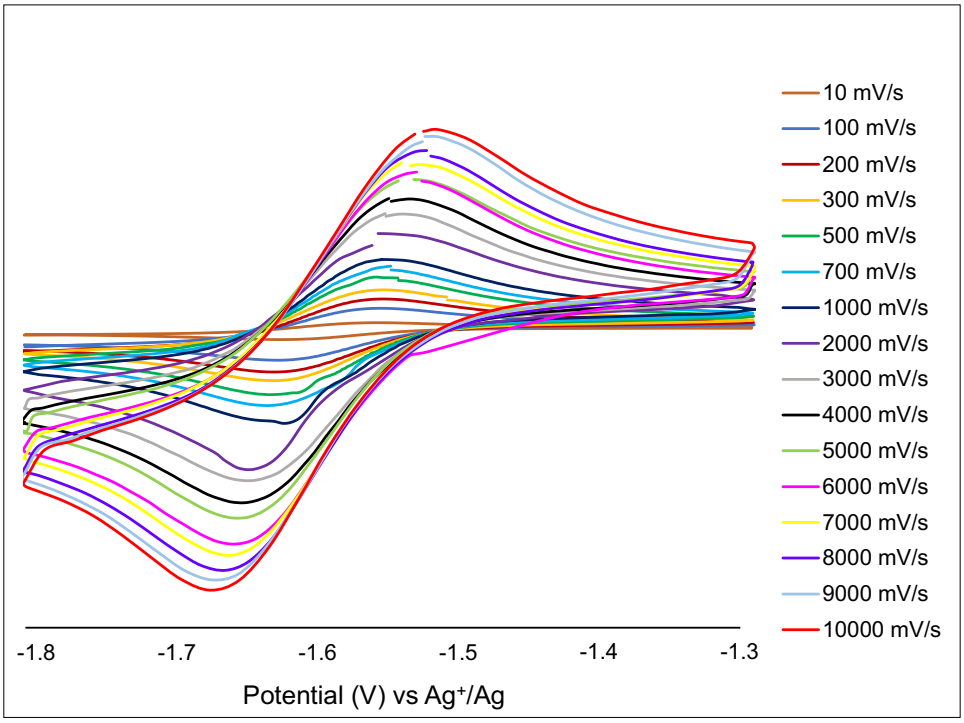

Figure S29. Cyclic voltammograms of **0/1**$^{-}$ redox couple at scan rates ranging from 10 – 10000 mV/s in 50:50 (v/v) MeCN:PC.

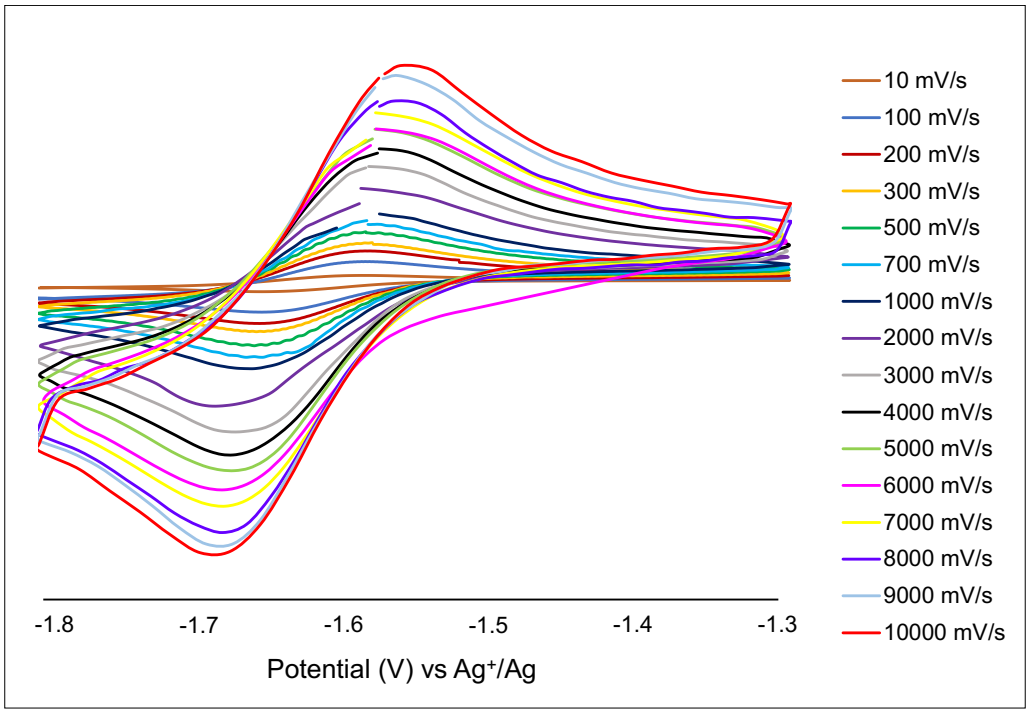

Figure S30. Cyclic voltammograms of **0/1**$^{-}$ redox couple at scan rates ranging from 10 – 10000 mV/s in 20:80 (v/v) MeCN:PC.

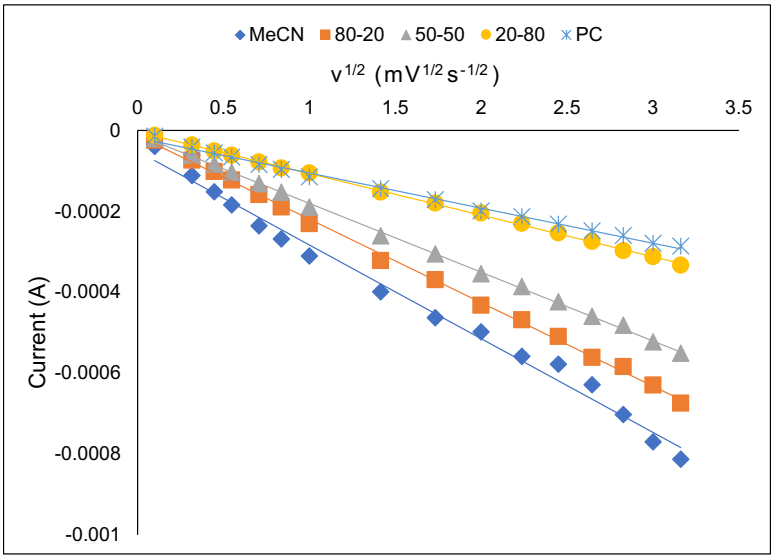

Figure S31. Plots of the square root of scan rate *versus* the peak current for **0/1**$^{-}$ redox couple in MeCN – PC mixtures. In the legend, the concentration of PC increases from left to right. For instance, ■ represents 80:20 (v/v) MeCN:PC mixture.

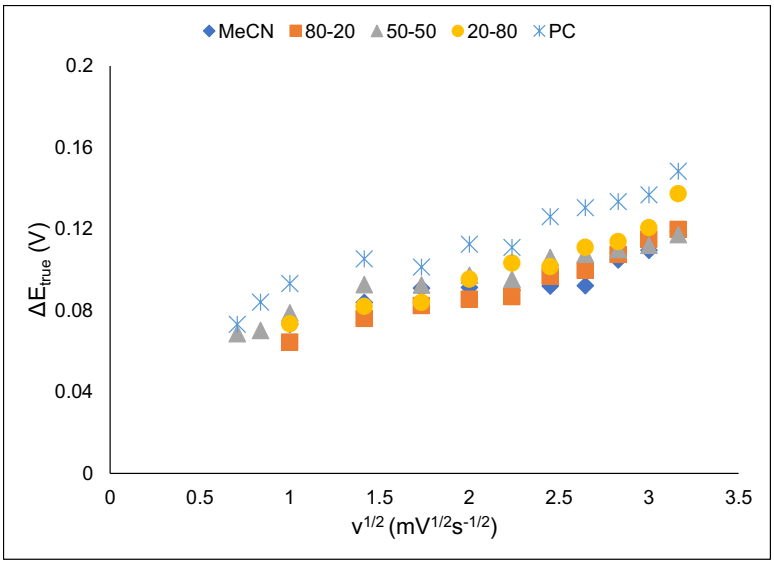

Figure S32. Plot of peak-to-peak separation (ΔE_p) *versus* square root of scan rate for $\mathbf{1}^+/\mathbf{0}$ redox couple in MeCN – PC mixtures. For each solvent, values are included for the scan rate range where $\Delta E_p > 64$ mV and increases as a function of scan rate. In the legend, the concentration of PC increases from left to right. For instance, ■ represents 80:20 (v/v) MeCN:PC mixture.

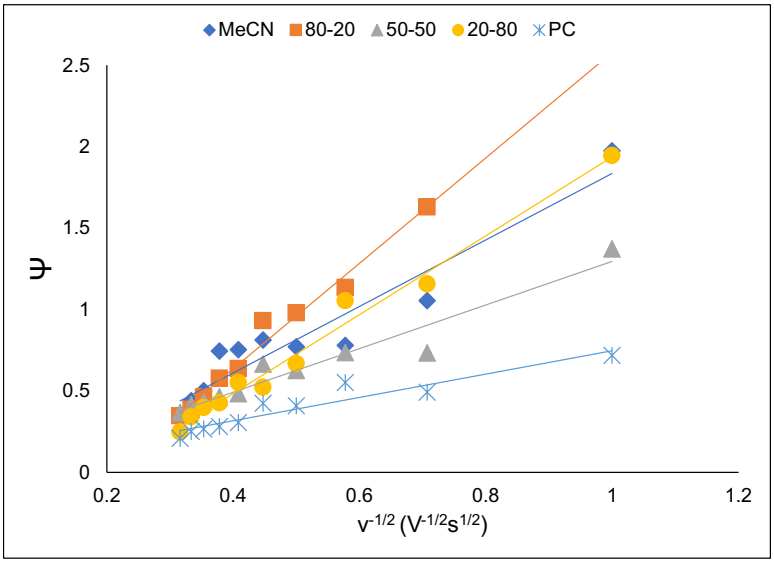

Figure S33. Plot of Nicholson parameter (Ψ) *versus* inverse square root of scan rate for $\mathbf{1}^+/\mathbf{0}$ redox couple in MeCN – PC mixtures. For each solvent, Ψ values corresponding to the given ΔE_p are included for scan rates where $\Delta E_p > 64$ mV. In the legend, the concentration of PC increases from left to right. For instance, ■ represents 80:20 (v/v) MeCN:PC mixture.

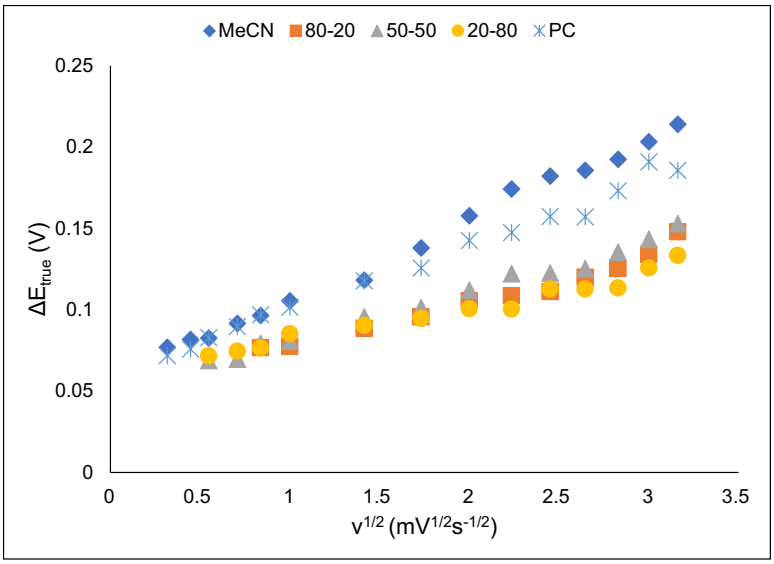

Figure S34. Plot of peak-to-peak separation (ΔE_p) *versus* square root of scan rate for **0/1**$^-$ redox couple in MeCN – PC mixtures. For each solvent, values are included for the scan rate range where $\Delta E_p > 64$ mV and increases as a function of scan rate. In the legend, the concentration of PC increases from left to right. For instance, ■ represents 80:20 (v/v) MeCN:PC mixture.

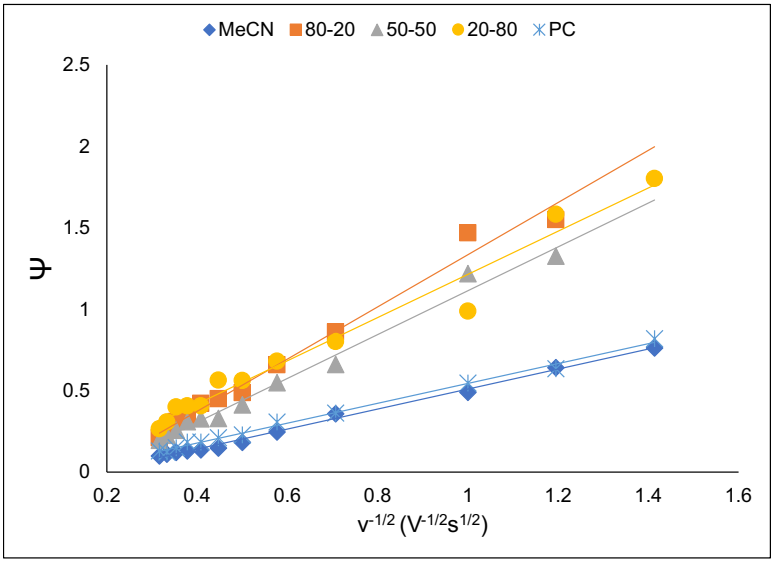

Figure S35. Plot of Nicholson parameter (Ψ) *versus* inverse square root of scan rate for **0/1**$^-$ redox couple in MeCN – PC mixtures. For each solvent, Ψ values corresponding to the given ΔE_p are included for scan rates where $\Delta E_p > 64$ mV. In the legend, the concentration of PC increases from left to right. For instance, ■ represents 80:20 (v/v) MeCN:PC mixture.

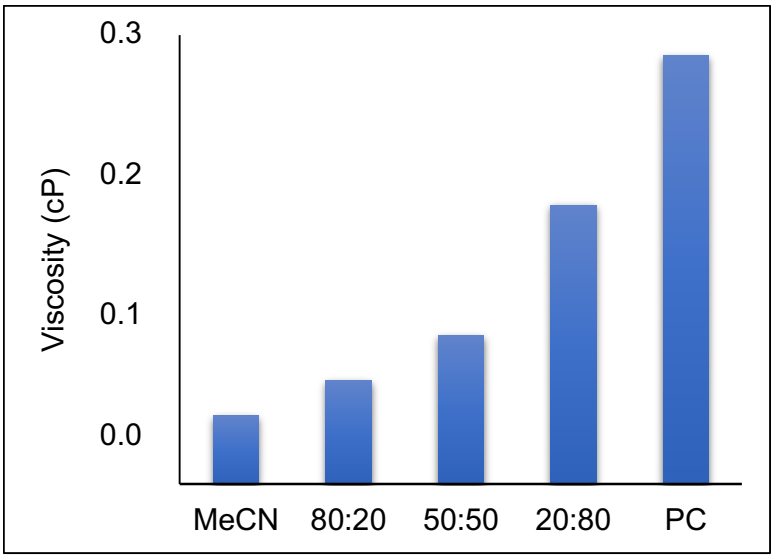

Figure S36. Viscosity of the electrolyte in MeCN – PC mixtures calculated using Stokes – Einstein equation. The concentration of PC increases from left to right.

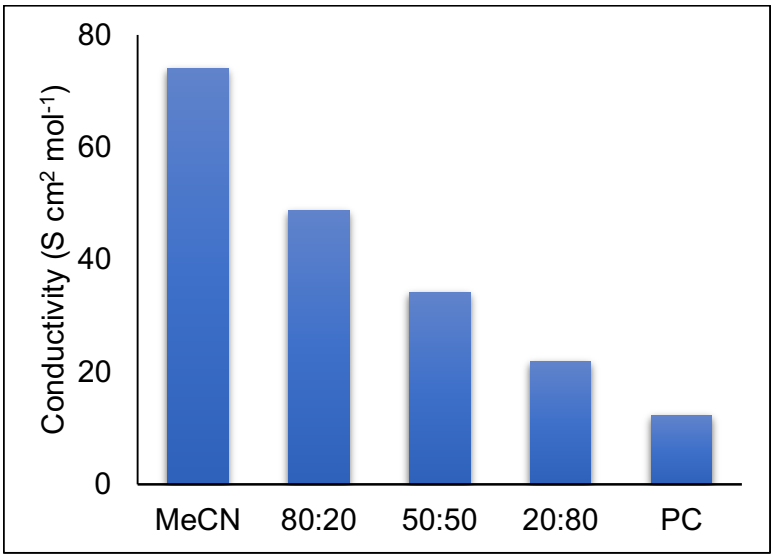

Figure S37. Conductivity of the electrolyte in MeCN – PC mixtures calculated using Stokes – Einstein equation. The concentration of PC increases from left to right.

Jouyban – Acree model

The Jouyban – Acree model gives a theoretical prediction of the influence of dynamic viscosity as a function of mole fraction of the studied solvent in binary mixtures.[6] It is a function of solvent physicochemical properties and estimates a positive or negative deviation from ideal liquid mixture behavior. The coefficients represent the weightage of a certain parameter in affecting the viscosity and they are calculated using regression analysis as explained in detail in the cited reference.

$$\ln(\eta_{m,T}) = \chi_1 \ln(\eta_{1,T}) + \chi_2 \ln(\eta_{2,T}) + \frac{\chi_1\chi_2}{T}[-61.784 + 54.566(E_{m1} - E_{m2})^2 - 129.759(S_1 - S_2)^2 - 1978.988(A_1 - A_2)^2 + 331.691(B_1 - B_2)^2 + 190.370(V_1 - V_2)^2] + \frac{\chi_1\chi_2(\chi_1 - \chi_2)}{T}[-706.352(A_1 - A_2)^2 + 65.119(V_1 - V_2)^2]$$

where $\eta_{m,T}$, $\eta_{1,T}$ and $\eta_{2,T}$ are viscosity of mixed solvents and pure solvents 1 and 2 at temperature T, χ_1 and χ_2 are the fractions of the solvents 1 and 2, E_m i s the excess molar refraction, S is polarizability of the analyte, A denotes the analyte's hydrogen-bond acidity, B stands for the analyte's hydrogen-bond basicity and V is the McGowan volume of the analytes.[6] The constants E_m, S, A, B, and V are known as the Abraham solvation parameters.[7]

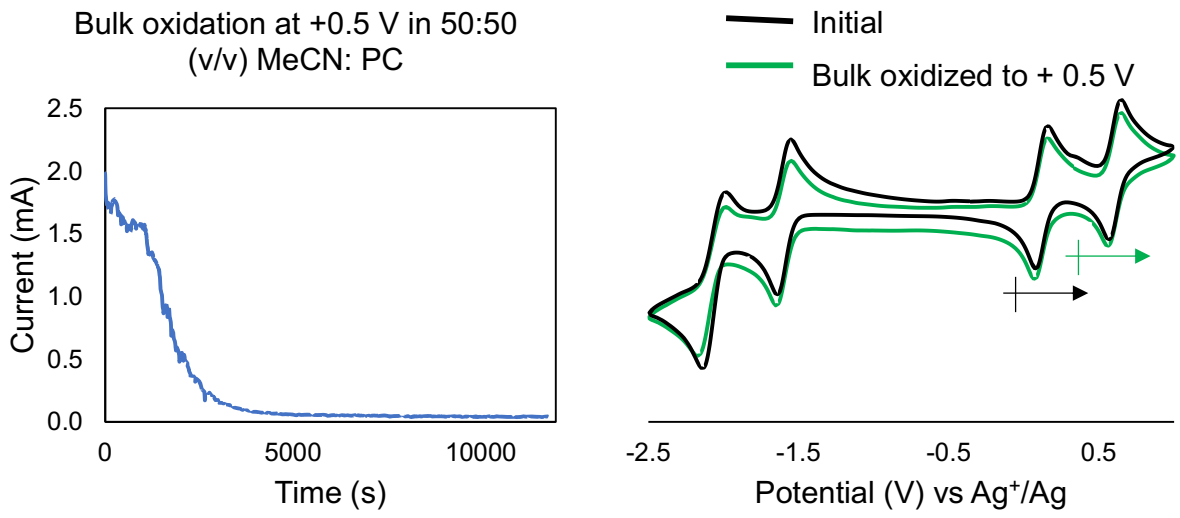

Figure S38. Bulk oxidation curves in 50:50 (v/v) MeCN – PC mixture (left); pre and post CV analysis of the electrolyte (right).

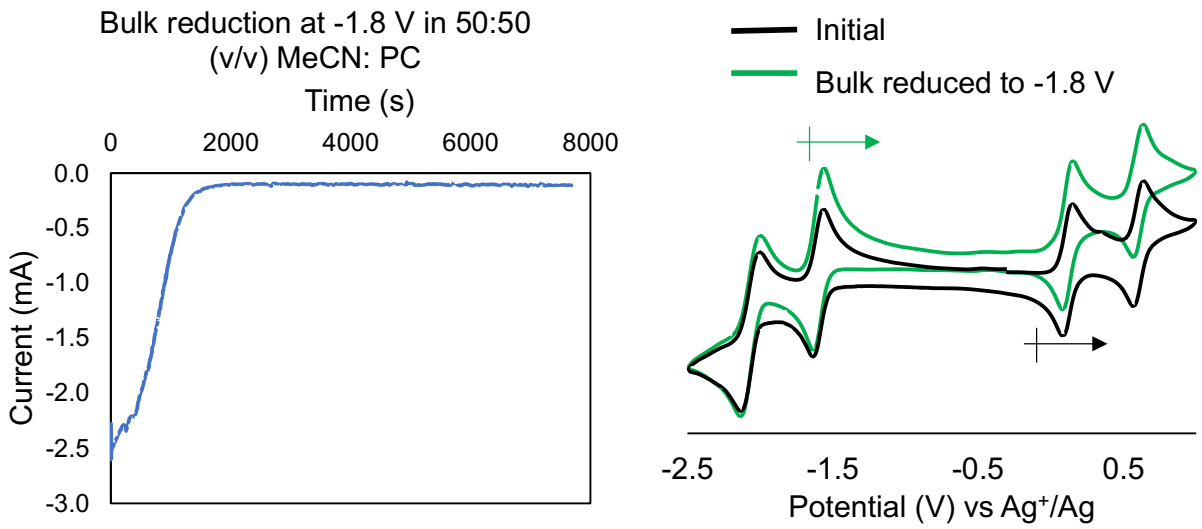

Figure S39. Bulk reduction curves in 50:50 (v/v) MeCN – PC mixture (left); pre and post CV analysis of the electrolyte (right).

Solubility measurements of $[Ti_2V_4O_5(OCH_3)_{14}]$

One of the major drawbacks to the limited success of existing electroactive materials for nonaqueous RFBs is poor solubility in organic solvent. Particularly, for polyoxometalate-based charge carrier, highly charged structures arise due to the oxo-bridged high-valent metal centers. The electron-donating bridging alkoxide ligands of the POV-alkoxides mitigate the necessity of accessing highly charged states by stabilizing the Lindqvist core through organic moieties. These surface ligands additionally enhance the solubility of the cluster in organic solvent. In the present study, the solubility of $[Ti_2V_4O_5(OMe)_{14}]$ was determined using electronic absorption spectroscopy in 0.1 M $[^nBu_4N][PF_6]$ solution in the desired solvent mixtures. We carried out these measurements for this report of the neutral form of the cluster as it is the least soluble form compared to the charged states. The solubility was observed to be the highest in the case of pure MeCN and decreases on gradual addition of PC.

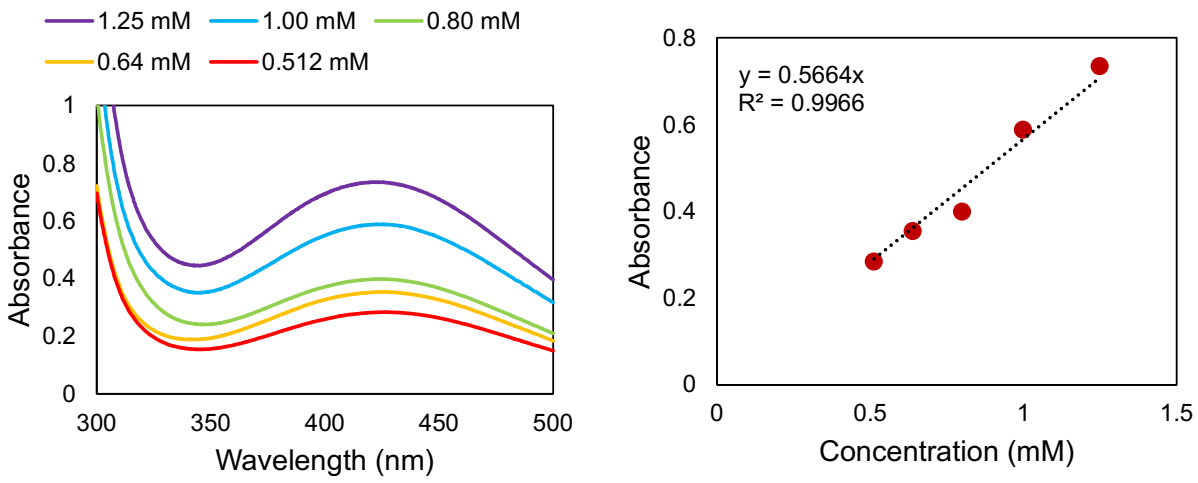

Figure S40. Solubility measurement of $[Ti_2V_4O_5(OMe)_{14}]$ in MeCN.

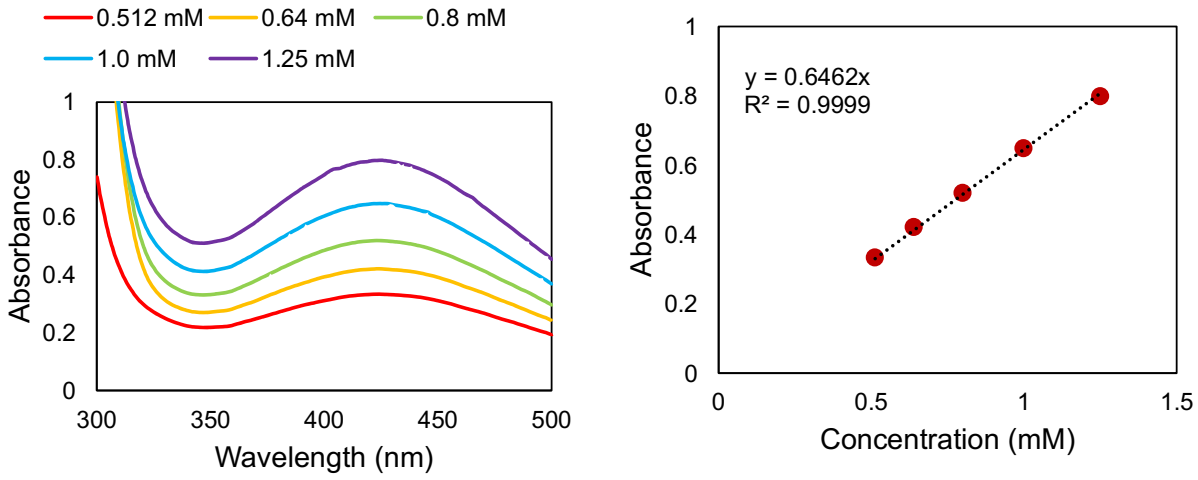

Figure S41. Solubility measurement of $[Ti_2V_4O_5(OMe)_{14}]$ in 80: 20 (v/v) MeCN: PC.

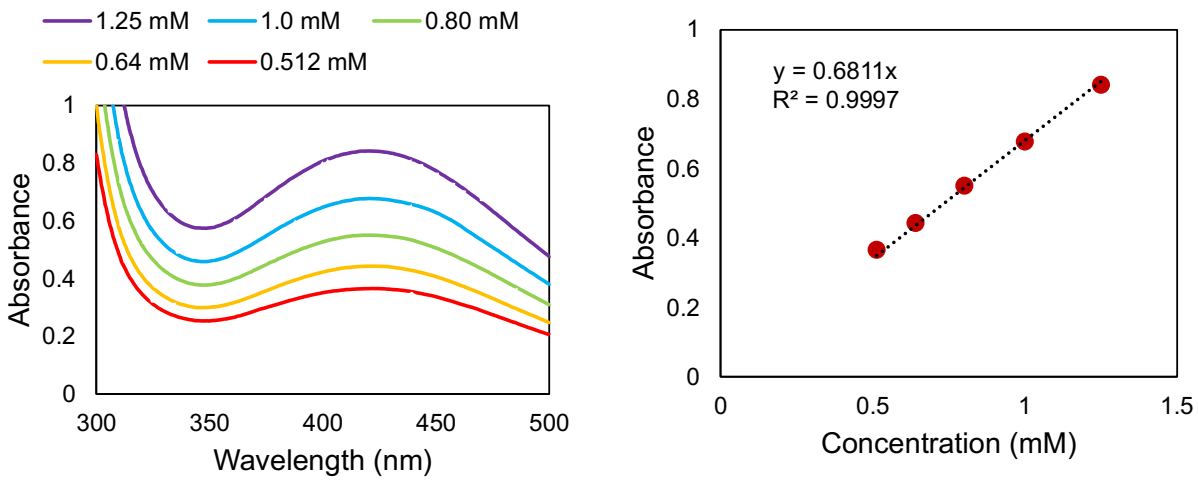

Figure S42. Solubility measurement of $[Ti_2V_4O_5(OMe)_{14}]$ in 50: 50 (v/v) MeCN: PC.

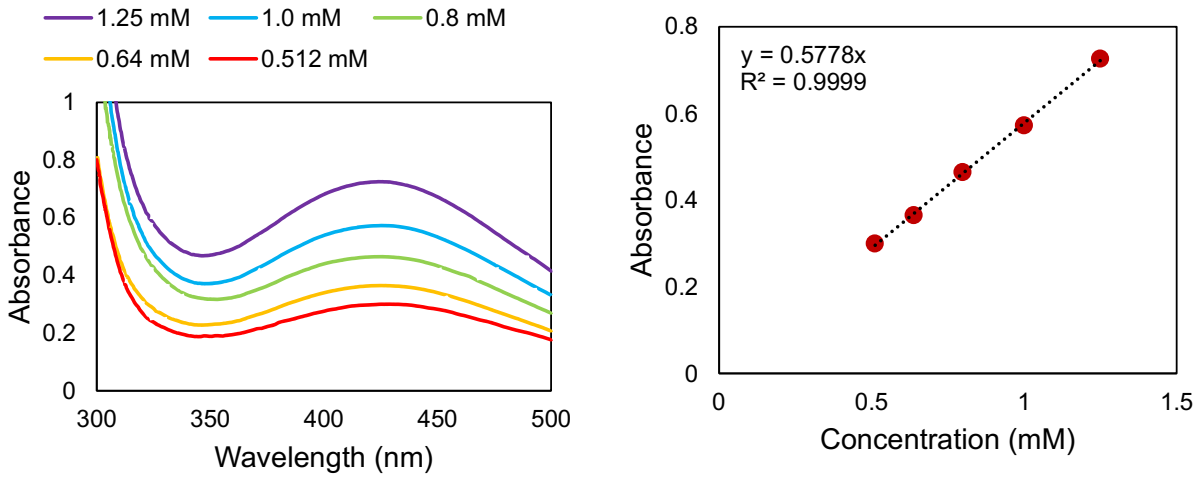

Figure S43. Solubility measurement of $[Ti_2V_4O_5(OMe)_{14}]$ in 20: 80 (v/v) MeCN: PC.

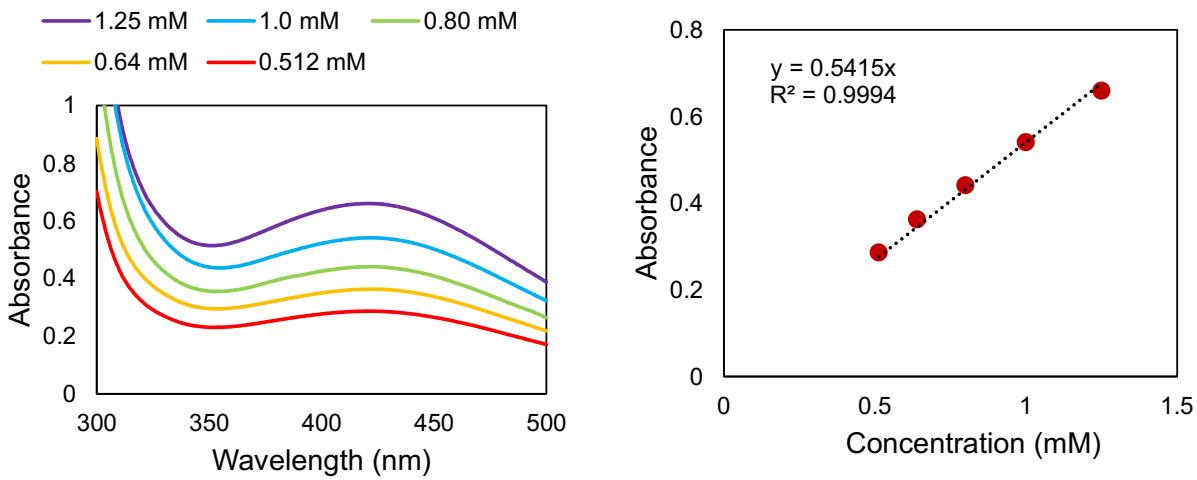

Figure S44. Solubility measurement of $[Ti_2V_4O_5(OMe)_{14}]$ in PC.

Table S3. Summary of solubility data of $[Ti_2V_4O_5(OMe)_{14}]$ in MeCN – PC mixtures.

Solvent mixtures	Extinction coefficient (cm^{-1} mM^{-1})	Dilute absorbances			Saturated concentrations (mM)			Solubility (mM)
		Trials			Trials			
		1	2	3	1	2	3	
MeCN	0.5664	0.816	0.936	0.903	40.77	46.82	45.15	44.25 ± 3.12
80 MeCN : 20 PC	0.6462	0.372	0.387	0.345	28.78	29.95	26.73	28.48 ± 1.63
50 MeCN : 50 PC	0.6811	0.539	0.536	0.586	26.94	26.80	29.32	27.69 ± 1.41
20 MeCN : 80 PC	0.5778	0.571	0.570	0.571	24.69	24.65	24.69	24.67 ± 0.03
PC	0.5415	0.449	0.450	0.448	20.76	20.79	20.69	20.75 ± 0.05

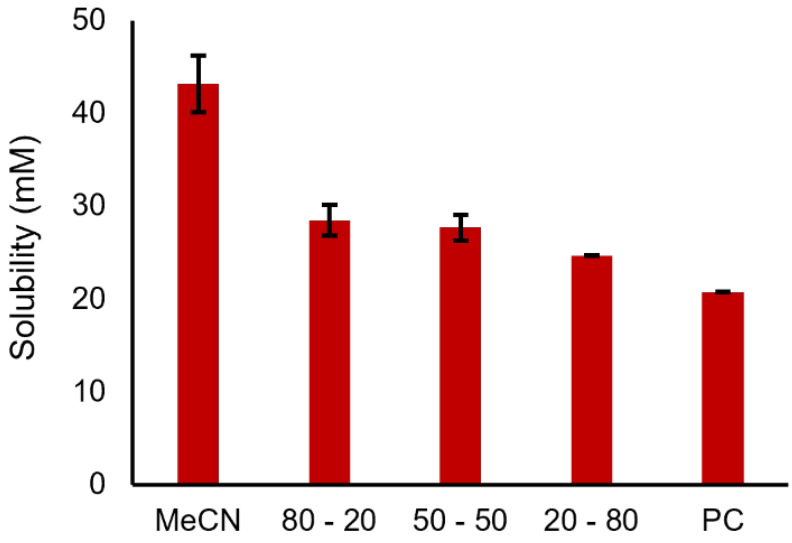

Figure S45. Mean solubility of $[Ti_2V_4O_5(OMe)_{14}]$ in different binary solvent ratios. The percentage of propylene carbonate increases from going left to right. The error bars denote the standard deviation observed during three replicates of each measurement.

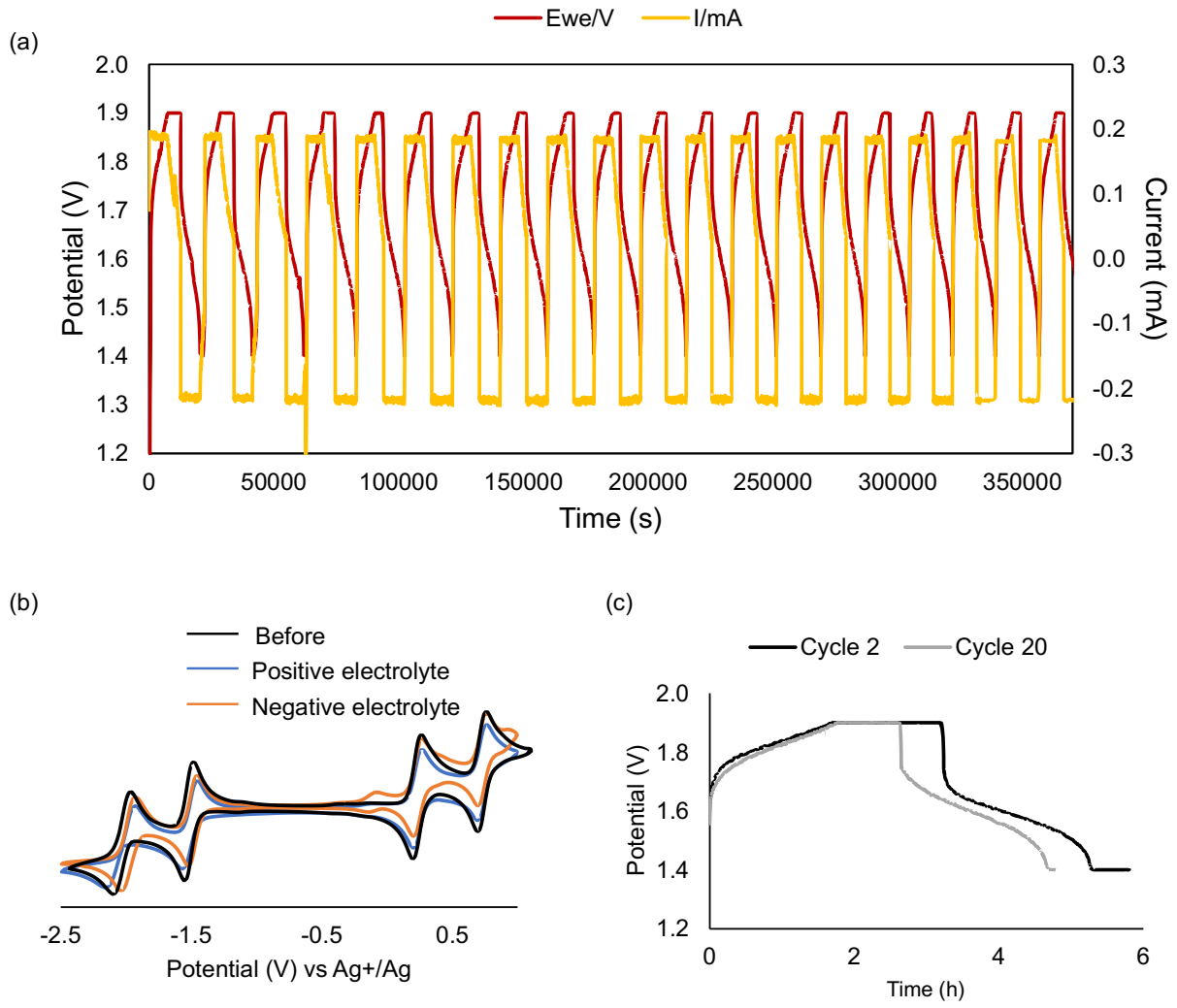

Figure S46. (a) Voltage trace of 20 cycles in charge – discharge cycling of $[Ti_2V_4O_5(OMe)_{14}]$ in MeCN (b) cyclic voltammograms of cluster before (black) and after charge-discharge cycles. The orange trace depicts the negative electrolyte whereas the blue trace denotes the positive electrolyte (c) Comparison of cycles 2 and 20 from the battery cycling experiment. All spurious responses in the battery cycling data are due to the stir bar getting stuck in between the carbon felt electrode(s) and the walls of the electrochemical cell.

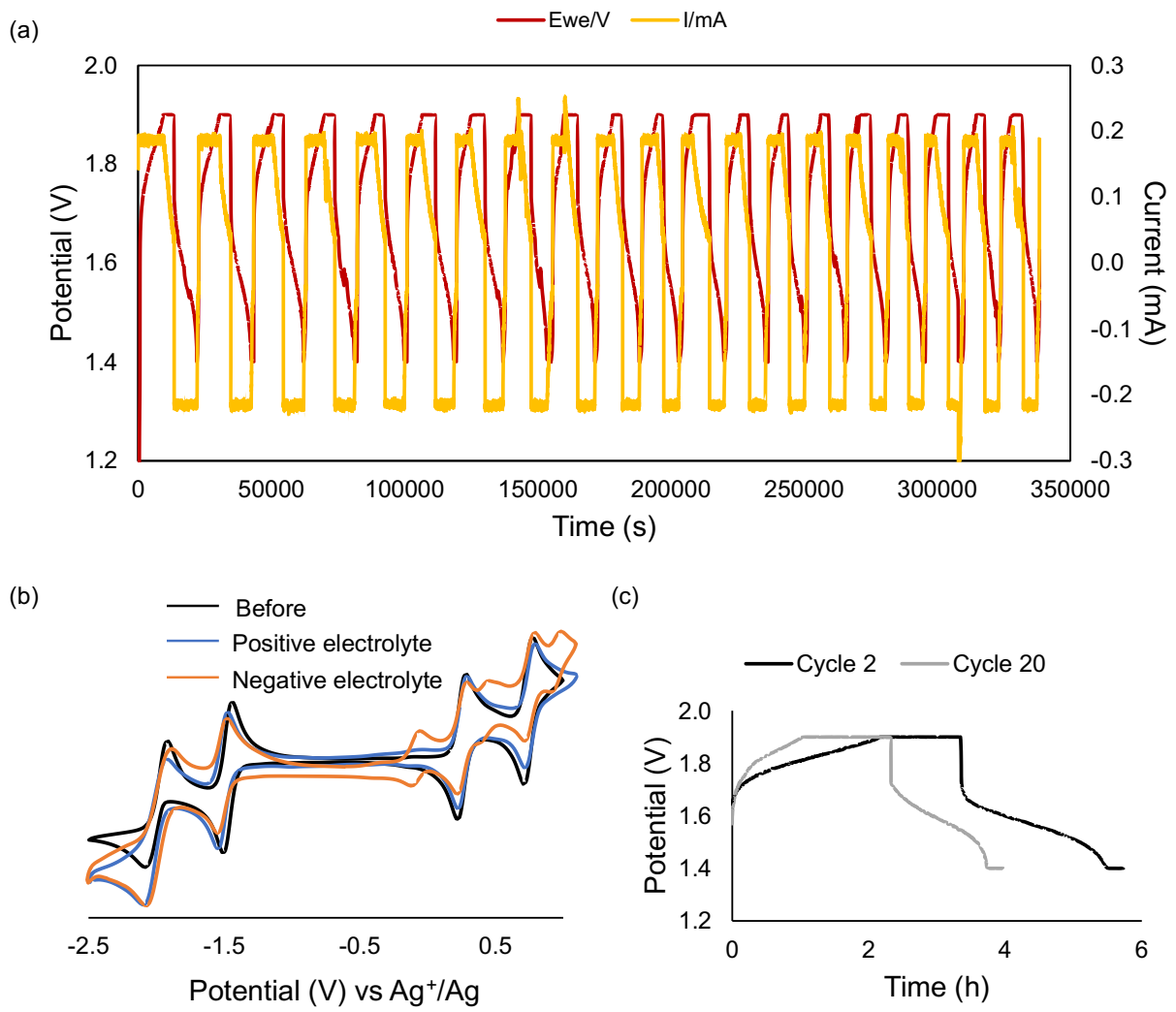

Figure S47. (a) Voltage trace of 20 cycles in charge – discharge cycling of $[Ti_2V_4O_5(OMe)_{14}]$ in 50:50 (v/v) MeCN: PC (b) cyclic voltammograms of cluster before (black) and after charge-discharge cycles. The orange trace depicts the negative electrolyte whereas the blue trace denotes the positive electrolyte (c) Comparison of cycles 2 and 20 from the battery cycling experiment. All spurious responses in the battery cycling data are due to the stir bar getting stuck in between the carbon felt electrode(s) and the walls of the electrochemical cell.

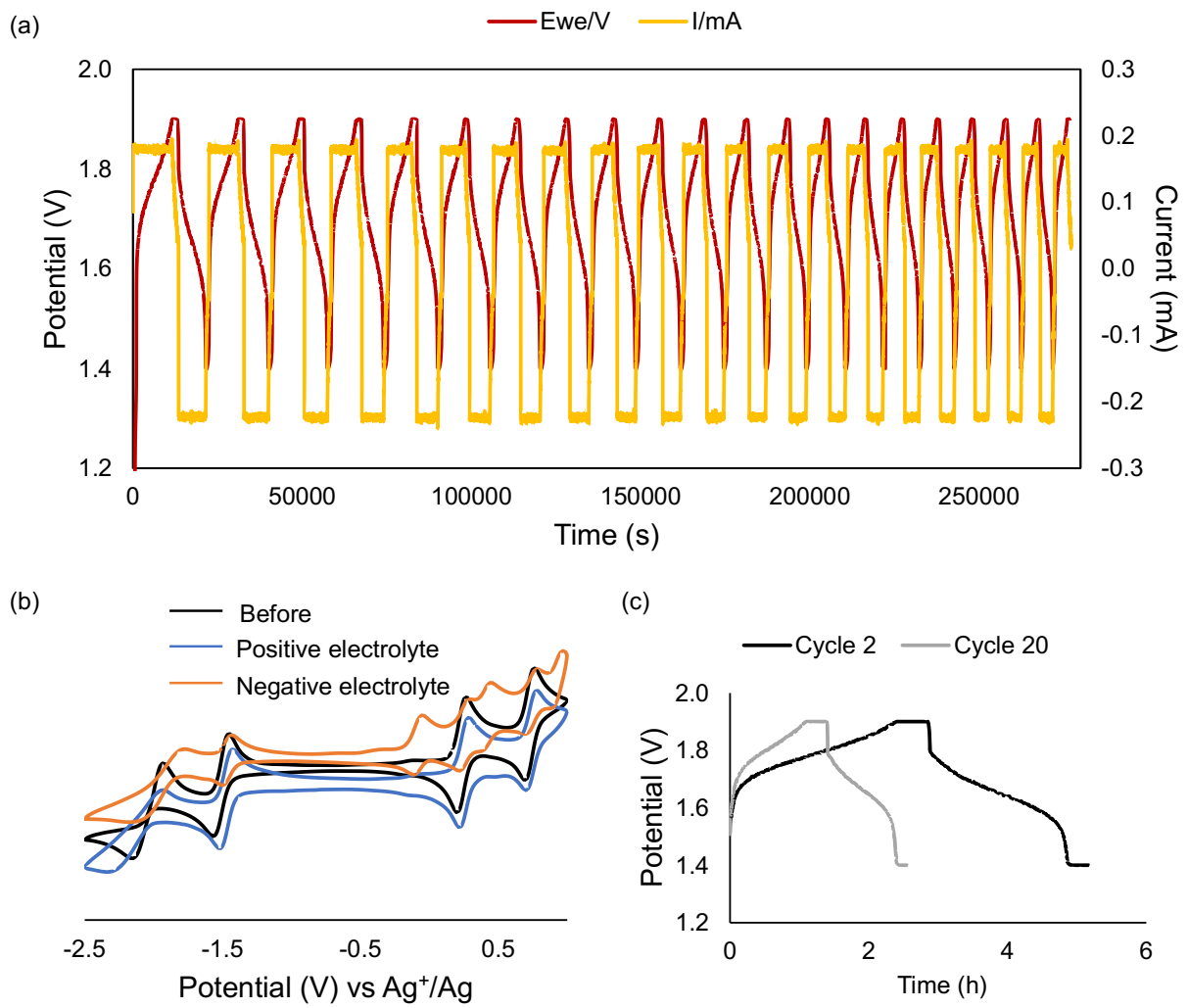

Figure S48. (a) Voltage trace of 20 cycles in charge – discharge cycling of $[Ti_2V_4O_5(OMe)_{14}]$ in 80:20 (v/v) MeCN: PC (b) cyclic voltammograms of cluster before (black) and after charge-discharge cycles. The orange trace depicts the negative electrolyte whereas the blue trace denotes the positive electrolyte (c) Comparison of cycles 2 and 20 from the battery cycling experiment.

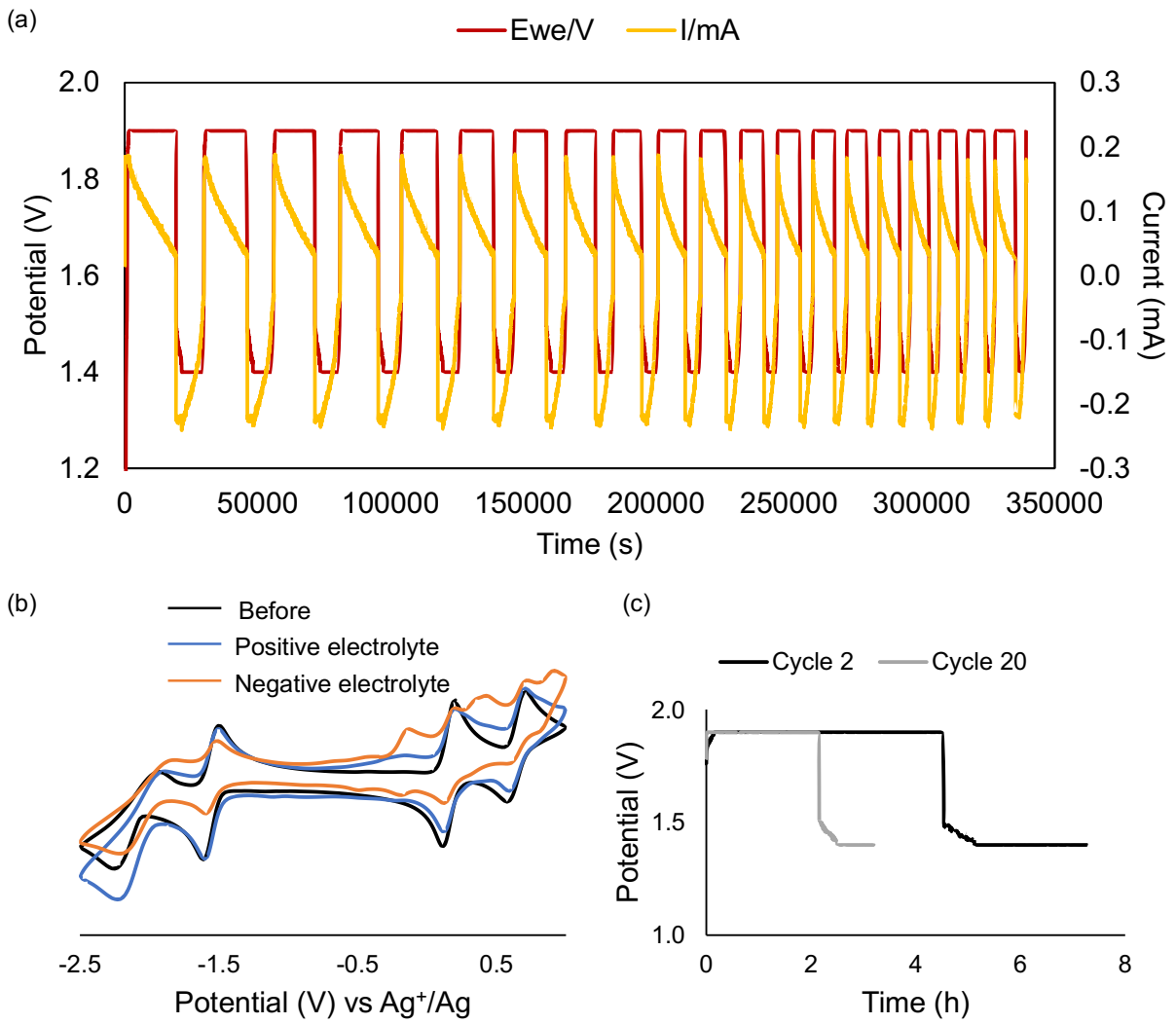

Figure S49. (a) Voltage trace of 20 cycles in charge – discharge cycling of $[Ti_2V_4O_5(OMe)_{14}]$ in PC (b) cyclic voltammograms of cluster before (black) and after charge-discharge cycles. The orange trace depicts the negative electrolyte whereas the blue trace denotes the positive electrolyte (c) Comparison of cycles 2 and 20 from the battery cycling experiment.

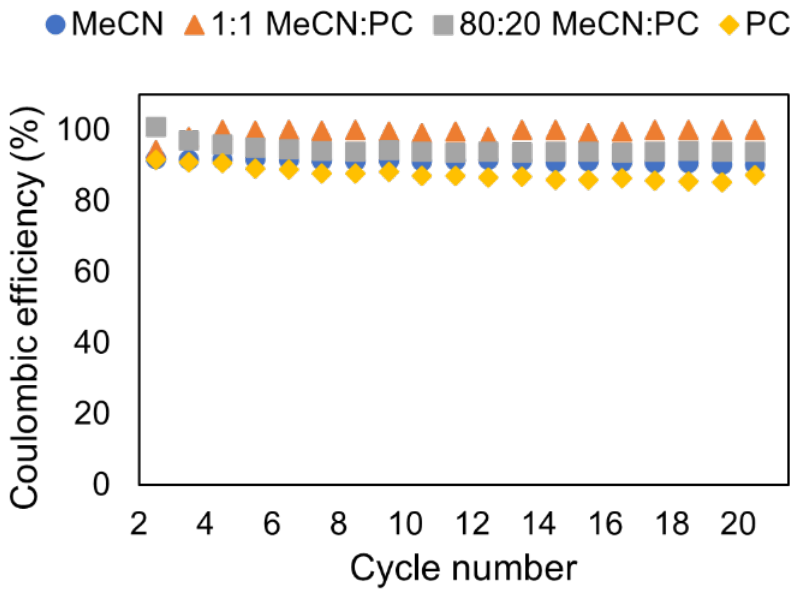

Figure S50. Columbic efficiency *versus* cycle number in MeCN – PC mixtures.

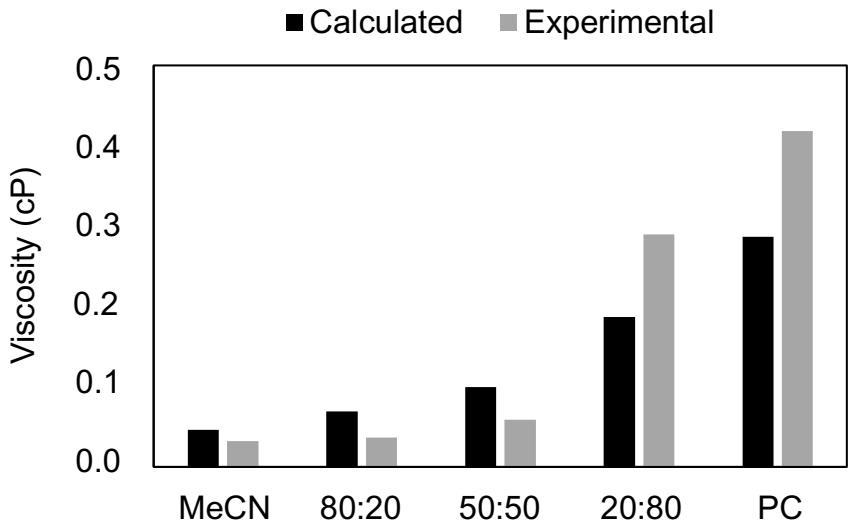

Figure S51. Experimentally determined viscosity values (grey) and the calculated viscosity using Stokes-Einstein equation (black) in MeCN – PC mixtures. The concentration of PC increases from left to right.

References

1. Vangelder, L. E.; Matson, M., Ellen Heterometal functionalization yields improved energy density for charge carriers in nonaqueous redox flow batteries. *Journal of Materials Chemistry A* **2018**, *6*, 13874-13882. DOI: 10.1039/c8ta03312a

2. Liu, Q. H.; Sleightholme, A. E. S.; Shinkle, A. A.; Li, Y. D.; Thompson, L. T. Non-aqueous vanadium acetylacetonate electrolyte for redox flow batteries. *Electrochemistry Communications* **2009**, *11*, 2312-2315. DOI: 10.1016/j.elecom.2009.10.006
3. Sleightholme, A. E. S.; Shinkle, A. A.; Liu, Q. H.; Li, Y. D.; Monroe, C. W.; Thompson, L. T. Non-aqueous manganese acetylacetonate electrolyte for redox flow batteries. *Journal of Power Sources* **2011**, *196*, 5742-5745. DOI: 10.1016/j.jpowsour.2011.02.020
4. Kosswattaarachchi, A. M.; VanGelder, L. E.; Nachtigall, O.; Hazelnis, J. P.; Brennessel, W. W.; Matson, E. M.; Cook, T. R. Transport and Electron Transfer Kinetics of Polyoxovanadate-Alkoxide Clusters. *Journal of the Electrochemical Society* **2019**, *166*, A464-A472. DOI: 10.1149/2.1351902jes
5. Nicholson, R. S. THEORY AND APPLICATION OF CYCLIC VOLTAMMETRY FOR MEASUREMENT OF ELECTRODE REACTION KINETICS. *Analytical Chemistry* **1965**, *37*, 1351-+. DOI: 10.1021/ac60230a016
6. Jouyban, A.; Maljaei, S. H.; Soltanpour, S.; Fakhree, M. A. A. Prediction of viscosity of binary solvent mixtures at various temperatures. *Journal of Molecular Liquids* **2011**, *162*, 50-68. DOI: 10.1016/j.molliq.2011.06.002
7. Flanagan, K. B.; Hoover, K. R.; Garza, O.; Hizon, A.; Soto, T.; Villegas, N.; Acree, W. E.; Abraham, M. H. Mathematical correlation of 1-chloroanthraquinone solubilities in organic solvents with the Abraham solvation parameter model. *Physics and Chemistry of Liquids* **2006**, *44*, 377-386. DOI: 10.1080/00319100600805448